J. Am. Chem. Soc. **1994,** *116,* 11898−11914

Density Functional/Poisson−Boltzmann Calculations of Redox Potentials for Iron−Sulfur Clusters

Jean-Marie Mouesca,* Jun L. Chen, Louis Noodleman,* Donald Bashford, and David A. Case

Contribution from the Department of Molecular Biology, The Scripps Research Institute, La Jolla, California 92037

Received January 31, 1994. Revised Manuscript Received September 22, 1994[⊗]

Abstract: Density functional calculations for 1Fe, 2Fe, and 4Fe iron−sulfur clusters are reported. From broken symmetry and high spin state calculations, the energies of the spin ground states can be calculated, along with spin Hamiltonian parameters J, B, and B' for Heisenberg coupling, resonance delocalization within a mixed valence pair, and resonance between pairs, respectively. Environmental effects are modeled through a continuum dielectric, so that the solvent contribution to the redox potential can be calculated. There is a good correlation between predicted and measured redox potentials. The concepts of spin and electron delocalization barycenter states are introduced, which are analogous to the ideas of ligand field stabilization theory, but now applied to spin coupling Hamiltonians. The Heisenberg spin coupling produces a negative redox potential shift for the 2Fe redox couple compared with one iron clusters. Both spin coupling and resonance delocalization contribute to the much higher redox potential found for the 4Fe high potential (HP$_{ox,red}$) couple compared to the reduced ferredoxin couple (Fd$_{ox,red}$) in synthetic analogues, and probably in proteins as well. The solvation contribution is large in all clusters and for all redox couples, but the calculations suggest that solvation mainly compensates for differences in electron−electron repulsion energies in vacuum. For the HP$_{ox}$ state, we find three low lying electronic states with redox potentials within 0.3 eV, which could contribute to the two redox potential peaks observed by differential pulse polarography. The HP$_{ox}$ clusters in synthetic systems and in proteins could involve any of these three states and are, therefore, probably more complicated than previously thought.

1. Introduction

Since many iron−sulfur proteins are electron transfer agents,[1] it is important to understand the fundamental basis for their general range of redox potentials as well as for variations among different proteins. Originally, this interest in redox properties was based on the prevalence of FeS electron transfer proteins involved in the electron transport chain in mitochondria, in photosynthetic electron transport, and in bacterial electron transport.[1] Here electron transfer is a largely reversible phenomena, although coupling to proton transfer may be involved. Each protein must be properly ordered by redox potential within the electron transport chain to minimize energy loss and electron trapping at intermediate points. Other FeS proteins are involved in catalytic electron transfer,[1] as in hydrogenases[2] nitrogenase,[3] and in coupled electron−proton transport, as in complex I (NADH-UQ oxidoreductase) in mitochondria.[4−6] More recently, the scope and relevance of electron transfer to iron−sulfur chemistry has been broadened by the recognition that irreversible electron transfer plays an important role in cluster conversion reactions.[7] For example, one electron cluster oxidation precedes 4Fe → 3Fe conversion with release of a labile Fe^{2+} ion.[2,7−9] A conversion cycle can be set up by adding one electron and Fe^{2+} to the oxidized 3Fe form, allowing the 4Fe cluster to be reconstituted in some cases. The biological relevance of this extends not only to cluster degradation and construction, but also to possible regulatory effects.

Numerous synthetic analogues for the active sites in iron−sulfur proteins have been prepared, with organic thiolates replacing cysteine.[10] Synthetic clusters display trends in redox potential (with respect to cluster size and oxidation state couple) which are broadly similar to those of the analogous proteins, although overall the proteins show more positive redox potentials. These shifts are largely due to differences in the protein electrostatic and dielectric environment (compared to the solvent environment of the synthetic systems), but there are also differences between thiolates and cysteine in terms of electron-donating ability. Nonetheless, we can begin to understand the complex redox properties of FeS proteins by first studying isolated FeS clusters in solution.

Clearly, the redox properties of iron−sulfur clusters in proteins and synthetic analogues are closely connected with their electronic structures, and with related questions of charge and spin distributions. Iron−sulfur systems are spin coupled, and the energy balance among different spin states can be delicate. For example, reduced 4Fe4S clusters often display coexisting $S = {}^1/_2$ and $S = {}^3/_2$ spin states.[11] We will show evidence, as

---

[⊗] Abstract published in *Advance ACS Abstracts,* December 1, 1994.

(1) Cammack, R. *Adv. Inorg. Chem.* **1992**, *38*, 281−322.

(2) Adams, M. W. W. *Adv. Inorg. Chem.* **1992**, *38*, 341−396.

(3) Burgess, B. K. In *Molybdenum Enzymes*; Spiro, T. G., Ed.; John Wiley: New York, 1985; pp 161−219.

(4) Beinert, H. *FASEB J.* **1990**, 2483−2491.

(5) Nicholls, D. G.; Ferguson, S. J. *Bioenergetics* 2; Academic Press: London, 1992.

(6) Silva, J. J. R.; Frausto, D.; Williams, R. J. P. *The Biological Chemistry of the Elements*; Clarendon Press: Oxford, 1991.

(7) Holm, R. H. *Adv. Inorg. Chem.* **1992**, *38*, 1−71.

(8) Kennedy, M. C.; Stout, C. D. *Adv. Inorg. Chem.* **1992**, *38*, 323−339.

(9) Roth, E. K. H.; Jordanov, J. *Inorg. Chem.* **1992**, *31*, 240−243.

(10) Holm, R. H.; Ibers, J. A. In *Iron-Sulfur Proteins*; Lovenberg, W., Ed.; Academic: New York, 1977; pp 205−281.

0002-7863/94/1516-11898$04.50/0

well, for near degeneracies among different electronic states in both reduced and in oxidized (high potential) 4Fe4S clusters. Electron delocalization and solvation effects can also affect spin equilibria.[2,12,13] The goal of the present work is to examine redox potentials with theoretical methods, and to relate our results to broader questions of electronic structure.

Here, we report the results of density functional calculations of redox potentials for FeS clusters with 1Fe, 2Fe, and 4Fe centers. We compare our results with experimental redox potentials measured for synthetic FeS clusters in various solvents. The approach that we have taken is (1) to calculate the electronic structure of the clusters using density functional methods, as one would for gas phase ions; (2) to calculate the molecular electrostatic potential (MEP) from the electron density; (3) to perform a least-squares fit of the calculated MEP to a set of point charges (the electrostatic potential charges, or ESP charges) centered on the atoms, and constrained to give the correct total molecular charge and dipole moment vector; and (4) to calculate, from the Poisson−Boltzmann equation, the solvent reaction field experienced by a continuous dielectric medium due to the ESP point charges, and subsequently, the energy of their interaction with the reaction field. This procedure is carried out for both oxidation states of the redox couple, and the difference in solvation energy between them is evaluated. The difference in solvation energy is then added to the gas phase ionization potential of the reduced species, IP(red), to obtain the absolute redox potential; a constant offset then produces a redox potential with respect to a reference electrode. Further analysis using the spin barycenter concept allows us to separate out the effects of Heisenberg spin coupling and of resonance delocalization coupling (double exchange) on the redox potential.

2. Methods

2.1. Overview. Redox potentials were calculated for the following FeS clusters: $[Fe(SCH_3)_4]^{2-,1-}$, $[Fe_2S_2(SCH_3)_4]^{3-,2-}$, $[Fe_4S_4(SCH_3)_4]^{1-,2-}$, and $[Fe_4S_4(SCH_3)_4]^{2-,3-}$. We will refer to these clusters by the number of iron atoms and the true cluster charges above. This differs from the usual convention of referring to the 2Fe2S or 4Fe4S core charge only, but redox potentials have a strong dependence on the true cluster charge, and it is worthwhile to focus on this. Alternatively, the 4Fe, 1−/2−, and 4Fe, 2−/3− redox couples will also be called $HP_{ox,red}$ and $Fd_{ox,red}$ to emphasize the oxidation state equivalence with high potential 4Fe4S proteins and with 4Fe4S ferredoxins, respectively. As is well known from the work of Carter,[14] HP_{red} and Fd_{ox} are equivalent oxidation states. For these calculations, the clusters are immersed in a solvent, modeled as a continuous dielectric of high dielectric constant. The solvent is then allowed to polarize in response to the cluster charge distribution, but the cluster is not allowed to polarize in response to the solvent. The standard redox potential (E^0) is calculated by adding the gas phase ionization potential for the reduced species (IP(red)) to the solvation energy difference for the oxidized minus the reduced state (ΔE_{PB}), and adding a known constant potential ($\Delta SHE = -4.5$ eV) to reference the "absolute" potential to the standard hydrogen electrode (SHE):

$$E^0 = IP(red) + \Delta E_{PB} + \Delta SHE \qquad (1)$$

Here we estimate IP(red) by density functional calculations and ΔE_{PB} by using classical electrostatics. Details of the approach are given in the following sections.

2.2. Density Functional Methods. All the calculations reported for the FeS clusters in vacuum utilized the Amsterdam LCAO Density Functional Programs (ADF) developed by Baerends and co-workers.[15−21] The local density approximation uses the exchange and correlation energy E_{XC}(LDA) given by Vosko, Wilk, and Nusair.[22,23] The Stoll correction for correlation energy[24,25] is added to this, along with Becke's[26,27] nonlocal correction for exchange energy, treated as a perturbation to E_{XC}(LDA) from the density of an LDA SCF calculation. We refer to this potential as VS+B to indicate that the Becke term is added perturbatively to the Vosko−Wilk−Nusair−Stoll potential. While fully self-consistent incorporation of nonlocal terms like the Becke term is more accurate, it is also more computationally taxing, and work by Fan and Ziegler shows that self-consistency effects on energies are rather small.[28] The bonding energies are calculated with respect to a reference state composed of the spin-restricted atoms constituting the molecule. Identical grids are used for the molecule and the atom fragments in the energy difference evaluation, and the electrostatic part of the interaction energy is calculated separately. These methods are a development of the earlier Ziegler−Rauk transition state method[29] and allow an accurate evaluation of total molecular energies. Matrix elements appearing in the secular equation are computed using a cellular integration method, with special rules within atomic spheres and Gauss product rules in the interstitial region, as developed by te Velde, Boerrigter, and Baerends.[16,30,31] Convergence was achieved when the change in the mean of the diagonal elements of the density matrix was less than 0.0003. The accuracy parameter for the numerical integration grid used was ACCINT = 3.5.

The molecular orbitals are expanded in an uncontracted double-ζ Slater-type orbitals (STO) basis set for all the atoms, with the 3d metal orbital for the iron using a triple-ζ basis set. Additional single-ζ polarization functions are added for Fe 4p, S 3d, and H 2p orbitals. All core orbitals are kept frozen and orthogonal to the valence orbitals. During the SCF cycle, the molecular densities are fit by a set of auxillary s, p, d, f, and g

---

(11) Meyer, J.; Moulis, J.-M.; Gaillard, J.; Lutz, M. *Adv. Inorg. Chem.* **1992**, *38*, 73−115.

(12) Noodleman, L.; Case, D. A. *Adv. Inorg. Chem.* **1992**, *38*, 423−470.

(13) Lindahl, P. A.; Day, E. P.; Kent, T. A.; Orme-Johnson, W. H.; Münck, E. J. *Biol. Chem.* **1985**, *260*, 11160−11173.

(14) Carter, C. W.; Kraut, J.; Freer, S. T.; Alden, R. A. *J. Biol. Chem.* **1974**, *249*, 6339−6346.

(15) *ADF (Aug., 1992)*, Department of Theoretical Chemistry, Vrije Universiteit, Amsterdam ().

(16) te Velde, G.; Baerends, E. J. *J. Comput. Phys.* **1992**, *99*, 84−98.

(17) Baerends, E. J.; Ellis, D. E.; Ros, P. *Chem. Phys.* **1973**, *2*, 41−59.

(18) Baerends, E. J.; Ros, P. *Int. J. Quantum Chem. Symp.* **1978**, *12*, 169−190.

(19) Bickelhaupt, F. M.; Baerends, E. J.; Ravenek, W. *Inorg. Chem.* **1990**, *29*, 350−354.

(20) Ravenek, W. In *Scientific Computing on Supercomputers*; Devreese, J. T., Van Camp, P. E., Eds.; Plenum: New York, 1989; pp 201−218.

(21) Ziegler, T. *Chem. Rev.* **1991**, *91*, 651−667.

(22) Vosko, S. H.; Wilk, L.; Nusair, M. *Can. J. Phys.* **1980**, *58*, 1200−1211.

(23) Painter, G. S. *Phys. Rev. B.* **1981**, *24*, 4264−4270.

(24) Stoll, H.; Pavlidou, C. M. E.; Preuss, H. *Theor. Chim. Acta* **1978**, *149*, 143−149.

(25) Stoll, H.; Golka, E.; Preuss, H. *Theor. Chim. Acta* **1980**, *55*, 29−41.

(26) Becke, A. D. *J. Chem. Phys.* **1986**, *84*, 4524−4529.

(27) Becke, A. D. In *The Challenge of d and f Electrons*; Salahub, D. R., Zerner, M. C., Ed.; American Chemical Society: Washington, DC, 1989; pp 165−179.

(28) Fan, L.; Ziegler, T. *J. Chem. Phys.* **1991**, *94*, 6057−6063.

(29) Ziegler, T.; Rauk, A. *Theor. Chim. Acta* **1977**, *46*, 1−10.

(30) Boerrigter, P. M.; te Velde, G.; Baerends, E. J. *Int. J. Quantum Chem.* **1988**, *33*, 87−113.

(31) te Velde, G. Numerical Integration and Other Methodological Aspects of Band Structure Calculations. Ph.D. Thesis, Vrije University, 1990.

Table 1. Geometrical Data[a]

systems	symmetry	Fe−Fe (Å)	Fe−S* (Å)	Fe−S (Å)	S−C (Å)	Fe−S*−Fe (deg)	S−Fe−S (deg)	S*−Fe−S* (deg)	Fe−S−R (deg)
$[Fe(SCH_3)_4]^{1-}$	C_{2v}			2.290	1.800		109.5		109.5
$[Fe(SCH_3)_4]^{2-}$	C_{2v}			2.360	1.800		109.5		109.5
$[Fe_2S^*_2(SCH_3)_4]^{2-}$	D_{2h}	2.690	2.210	2.310	1.800	75.0	109.5	105.0	109.5
$[Fe_2S^*_2(SCH_3)_4]^{3-}$									
HS	D_{2h}	2.730	2.244	2.345	1.800	74.9	109.5	105.1	109.5
BS	C_{2v}	2.730	2.279	2.380	1.800	74.9	109.5	102.8	109.5
			2.210	2.310	1.800	74.9	109.5	107.4	109.5
$[Fe_4S^*_4(SCH_3)_4]^{2-}$									
"Holm"	D_{2d}	2.775(×2)	2.310(×8)	2.251	1.832	73.8		104.1	103.0
		2.733(×4)	2.241(×4)	2.251	1.832	73.8		104.1	103.0
$[Fe_4S^*_4(SCH_3)_4]^{3-}$									
"relaxed"	D_{2d}	2.743(×2)	2.291(×8)	2.295	1.832	72.9		104.8	103.0
		2.743(×4)	2.352(×4)	2.295	1.832	72.9		104.8	103.0
$[Fe_4S^*_4(SCH_3)_4]^{1-}$									
"Holm"	D_{2d}	2.775(×2)	2.310(×8)	2.251	1.832	73.8		104.1	103.0
		2.733(×4)	2.241(×4)	2.251	1.832	73.8		104.1	103.0
"Millar"	C_{2v}	2.754(×1)	2.271(×4)	2.209	1.927	74.6		103.9	109.5
		2.724(×1)	2.279(×4)	2.204	1.862	73.4		105.1	109.5
		2.740(×4)	2.234(×4)						

[a] For 1Fe, see refs 41−46; 2Fe, refs 47−51; 4Fe, refs 42, 52−54. See text for further discussion of geometries.

STO functions, centered on all nuclei, which generate the Coulomb and exchange and correlation potentials. These fitted STO functions are used to evaluate the electrostatic potentials at any point in space around the clusters. Basis sets, core sets, core coefficients, and fit sets are included as supplemental material.

2.3. Charge Fitting and Solvation Energies. The ESP charges were obtained by merging the Amsterdam density functional codes with the code CHELPG of Breneman and Wiberg,[32] which is a development of the earlier work of Chirlian and Francl[33] and Besler *et al.*[34] Two modifications of this code were made to yield improved ESP charges: (1) the three Cartesian components of the dipole moment were used as constraint equations on the ESP charges, along with the total charge constraint equation; (2) grid points were constructed symmetrically about the origin in each Cartesian direction. The box size is slightly adjusted in x,y,z so that an integer number of points is found in $\pm x, \pm y, \pm z$. Symmetry equivalent atoms are then treated so that their ESP charges are equivalent. In place of the standard Gauss−Jordan matrix inversion, we used singular value decomposition[35] as described in the Appendix. This has the advantage of testing the stability of the charges and solvation energies.

The ESP charges were then substituted into the program SOLVATE, which is one element of the MEAD (Macroscopic Electrostatics with Atomic Detail) suite of programs developed by D. Bashford.[36−38] In this approach, the solute−solvent interaction is treated within the framework of classical electrostatics. The solute is represented by a set of atomic charges and Born radii, and the solvent as a continuous dielectric medium. The dielectric boundary between the interior and the exterior is defined by the surface of contact of a 1.4 Å sphere rolling over the superposition of spheres defined by the Born radii of the atoms. The free energy difference for charging the solute in vacuum and in solution is calculated by solving the macroscopic Poisson equation using a finite difference method and a standard overrelaxation algorithm to obtain the reaction field potential ϕ^R for each oxidation state.[36−38] Then,

$$\Delta E_{PB} = {}^1/_2\Big(\sum_j q_j^{ox}\phi_j^R(ox)\Big) - {}^1/_2\Big(\sum_j q_j^{red}\phi_j^R(red)\Big) \qquad (2)$$

where the field points for the reaction field are evaluated at the point charge positions (positions of the nuclei) for the solvation energy evaluation. More details of this approach and its biological and chemical applications can be found in recent review articles.[36−40]

In CHELPG, the outer atomic radius on each atom was set to 5.0 Å, and the grid spacing to 0.2 Å. For each atom, sampling points are determined by taking all those points on a cubic grid lying between the Born radius and the outer atomic radius centered on that atom. The Born radii used for the various atoms are as follows: Fe, 1.5 Å; S, 1.8 Å; C, 1.67 Å; H, 1.32 Å. The Poisson−Boltzmann equation was solved at zero ionic strength on three successively finer grids with spacings of 1.0, 0.25, and 0.15 Å and sizes of 61^3, 61^3, and 81^3, respectively.

2.4. Geometries. The geometries used are summarized in Table 1, and some aspects of the choices we made are discussed here.

1Fe Clusters. For both oxidized and reduced states, we chose a C_{2v} symmetry: the core itself FeS_4 is of T_d symmetry (the six S−Fe−S angles have the same value of 109.5°). The oxidized and reduced models differ only by the Fe−S bond length: 2.29 Å for the former and 2.36 Å for the latter. This is in accord with previous theoretical calculations,[41,42] and is consistent with typical experimental geometries. For example, the bond lengths for different reduced species from synthetic analogs are 2.36 Å for $[Fe(S_2\text{-}o\text{-}xyl)_2]^{2-}$ and $Fe[(SPMe_2)_2N]_2$, and 2.34 Å for $[Fe(S\text{-}2\text{-}(Ph)C_6H_4)]^{2-}$.[43−46]

2Fe Clusters. For the oxidized 2Fe ferredoxin cluster, the two halves have been taken as identical, by averaging different

---

(32) Breneman, C. M.; Wiberg, K. B. *J. Comput. Chem.* **1990**, *11*, 361−373.

(33) Chirlian, L. E.; Francl, M. M. *J. Comput. Chem.* **1987**, *8*, 894−905.

(34) Besler, B. H.; Merz, K. M., Jr.; Kollman, P. A. *J. Comput. Chem.* **1990**, *11*, 431−439.

(35) Press, W. H.; Flannery, B. P.; Teukolsky, S. A.; Vetterling, W. T. *Numerical Recipes. The Art of Scientific Computing*; Cambridge University Press: Cambridge, 1986.

(36) Lim, C.; Bashford, D.; Karplus, M. *J. Phys. Chem.* **1991**, *95*, 5610−5620.

(37) Bashford, D.; Gerwert, K. *J. Mol. Biol.* **1992**, *224*, 473−486.

(38) Bashford, D. *Curr. Op. Struct. Biol.* **1991**, *1*, 175−184.

(39) Bashford, D.; Karplus, M. *Biochemistry* **1990**, *29*, 10219−10225.

(40) Honig, B.; Sharp, K.; Yang, A.-S. *J. Phys. Chem.* **1993**, *97*, 1101−1109.

(41) Norman, J. G., Jr.; Jackels, S. C. *J. Am. Chem. Soc.* **1975**, *97*, 3833−3835.

(42) Noodleman, L.; Norman, J. G., Jr.; Osborne, J. H.; Aizman, A.; Case, D. A. *J. Am. Chem. Soc.* **1985**, *107*, 3418−3426.

(43) Lane, R. W.; Ibers, J. A.; Frankel, R. B.; Papaefthymiou, G. C.; Holm, R. H. *J. Am. Chem. Soc.* **1977**, *99*, 84−98.

(44) Churchill, M. R.; Wormald, J. *Inorg. Chem.* **1971**, *10*, 1778−1782.

geometries of synthetic analogues[47,48] so that the overall geometry is D_{2h}. For the reduced cluster, we followed the model presented earlier,[49-51] where the Fe–S* as well as the Fe–S(ligand) bond lengths have been increased by 0.07 Å at the reduced Fe site, and the Fe–Fe distance increased from 2.69 Å (oxidized model) to 2.73 Å. We therefore have an overall symmetry of C_{2v}. To perform "high-spin" calculations (where the monomer spins are parallel or "ferromagnetically" aligned), we kept the same geometry for the oxidized model and constructed an average geometry of symmetry D_{2h} in the reduced case, averaging the dimensions over the two subunits (resulting in Fe–S* = 2.245 Å and Fe–S = 2.345 Å, while Fe–Fe remained fixed at 2.73 Å.)

4Fe Clusters. Three geometries have been considered. The first one was used for the 2- and 1- oxidation states and is based on an idealization of the experimental structure of the tetraethylammonium salt of $[Fe_4S^*_4(SCH_2Ph)_4]^{2-}$.[52] This structure has an axis of compression resulting in four "short" (2.24 Å) and eight "long" (2.31 Å) Fe–S* distances. The overall nuclear framework has D_{2d} symmetry.

To treat the reduced ferredoxin cluster, we considered a second geometry that has a general expansion of the core, as is observed experimentally in $[Fe_4S^*_4(SPh)_4]^{3-}$.[53] This also has D_{2d} symmetry, but with eight "short" (2.29 Å) and four "long" (2.35 Å) Fe–S* distances.[42] The third geometry, relevant to the oxidized high potential clusters, is based on the crystallographic compound $[Fe_4S_4(S\text{-}2,4,6\text{-}(i\text{-}Pr)_3C_6H_2)_4]^{1-}$ [54] with C_2 symmetry, from which we constructed a model with C_{2v} symmetry. The main difference between the original and modified coordinates lies in the fact that, in the latter, the sequence C–S–Fe–Fe–S–C is constrained to be planar. The Fe–Fe distances now follow a 1:1:4 pattern where the four distances are averages of the original distances (two at 2.73, two at 2.75 Å). The Fe–S* were also averaged 2 by 2 to obtain an overall C_{2v} geometry.

3. Effects of Spin Coupling

The iron–sulfur clusters considered here are spin-coupled systems. As in previous work,[12] we represent the antiferromagnetic spin-coupled state in density functional theory by a "broken symmetry" state, where a spin-unrestricted determinant is constructed in which the spin-up electrons are predominantly on one-half of the molecule, and the spin-down electrons on the other half. A "high-spin" determinant can also be constructed where the spins on the two halves of the cluster are aligned in a parallel fashion. These density functional energies can then be fit to an appropriate spin Hamiltonian to obtain estimates of standard coupling and delocalization parameters, as well as estimates of the energies of the entire manifold of possible pure-spin states. Here we present details of how this approach is applied to 2Fe and 4Fe systems.

Let us focus first on the "broken symmetry" state. This can be considered as a weighted average of pure-spin states, the weights being the Clebsch–Gordan coefficients relating the spin quantum numbers for oppositely aligned spin vectors of the subunits to the total spin quantum number. It turns out that the energy difference between the high-spin and broken-symmetry states can be expressed in a general way when a Heisenberg Hamiltonian is applicable, that is if

$$H_{\text{spin}} = J\hat{S}_A\cdot\hat{S}_B \tag{3}$$

where S_A and S_B refer either to *monomer* spin quantum numbers (for oxidized and reduced dimers) or equivalently to *pair* spin quantum numbers (for tetramers within a pairwise spin coupling scheme). Representing the spin operator product as

$$\hat{S}_A\cdot\hat{S}_B = (S_{A+}S_{B-} + S_{A-}S_{B+})/2 + S_{Az}S_{Bz} \tag{4}$$

and representing by an outer product of the form $|S_AM_A\rangle\,|S_BM_B\rangle$ both the high-spin state (HS: $M_A = +S_A$, $M_B = +S_B$) and the broken-symmetry state (BS: $M_A = +S_A$, $M_B = -S_B$) we then take the expectation values

$$\langle\hat{S}_A\cdot\hat{S}_B\rangle_{\text{HS}} = +S_AS_B$$

$$\langle\hat{S}_A\cdot\hat{S}_B\rangle_{\text{BS}} = -S_AS_B \tag{5}$$

Only the term $S_{Az}S_{Bz}$ contributes, with the other two terms involving the raising and lowering operators giving zero when the expectation value is taken either from the broken-symmetry or high-spin state. Equation 5 leads directly to

$$E(S_{\max}{=}S_A{+}S_B) - E_{\text{B}}(M_S{=}|S_A{-}S_B|) = 2JS_AS_B \tag{6}$$

for the energy difference between the high-spin and broken-symmetry states. Energy differences of this sort are collected in Table 2 for a variety of clusters, and the resulting spin Hamiltonian parameters are collected in Table 3. The following paragraphs discuss the effects of this spin coupling for two- and four-iron clusters.

3.1. 2Fe2S Systems. The spin Hamiltonian used to treat the case of the 2Fe2S homonuclear ferric dimer is simply

$$H = J_{\text{ox}}\hat{S}_1\cdot\hat{S}_2 \tag{7}$$

with monomer spin quantum numbers $S_1 = S_2 = {}^5/_2$. The relevant equations for that system, allowing us to determine the value of J_{ox} as well as the position of the $S_{\min} = 0$ spin ground state, are given in Table 2. In the case of the mixed valence dimer (2Fe2S reduced with $S_1 = {}^5/_2$ and $S_2 = 2$) a complication arises. The high spin state is delocalized so that, for the sixth d electron, both σ_g and σ_u molecular orbitals are possible for the highest energy $S_{\max} = {}^9/_2$ state. For a completely delocalized dimer, the appropriate spin Hamiltonian is given by

$$H = J_{\text{red}}\hat{S}_1\cdot\hat{S}_2 \pm B(S + {}^1/_2) \tag{8}$$

where S is the total spin, and B is the resonance delocalization (hopping) parameter for the sixth d electron which multiplies $S + {}^1/_2$ to give the delocalization energy. Since the calculated high-spin state is delocalized (lower g root) its energy by density functional theory corresponds to $E(S_{\max})_g = (J_{\text{red}}/2)S_{\max}(S_{\max} + 1) - B(S_{\max} + {}^1/_2)$. It is then useful to define an average pure-spin state $E(S)_{\text{av}(B)}$ where the B resonance term has been averaged over the g and u resonance states. We obtain $E(S_{\max})_{\text{av}(B)}$ by adding $B(S_{\max} + {}^1/_2)$ to the energy of the state $E(S_{\max})_g$. The value of B is determined from the orbital energy difference $10B = E(S_{\max})_u - E(S_{\max})_g$ between the g and u roots.

---

(45) Coucouvanis, D.; Swenson, D.; Baenziger, N. C.; Holah, D. G.; Kostikas, A.; Simopoulis, A.; Petroleas, V. *J. Am. Chem. Soc.* **1976**, *98*, 5721–5723.

(46) Gebhard, M. S.; Koch, S. A.; Millar, M.; Devlin, F. J.; Stephens, P. J.; Solomon, E. I. *J. Am. Chem. Soc.* **1991**, *113*, 1640–1649.

(47) Mayerle, J. J.; Denmark, S. E.; Pamphilis, B. V. De; Ibers, J. A.; Holm, R. H. *J. Am. Chem. Soc.* **1975**, *97*, 1032–1045.

(48) Holm, R. H. *Acc. Chem. Res.* **1977**, *10*, 427–434.

(49) Norman, J. G., Jr.; Kalbacher, B. J.; Jackels, S. C. *J. Chem. Soc., Chem. Commun.* **1978**, 1027–1029.

(50) Norman, J. G., Jr.; Ryan, P. B.; Noodleman, L. *J. Am. Chem. Soc.* **1980**, *102*, 4279–4282.

(51) Noodleman, L.; Baerends, E. J. *J. Am. Chem. Soc.* **1984**, *106*, 2316–2327.

(52) Averill, B. A.; Herskovitz, T.; Holm, R. H.; Ibers, J. A. *J. Am. Chem. Soc.* **1973**, *95*, 3523–3534.

(53) Berg, J. M.; Hodgson, K. O.; Holm, R. H. *J. Am. Chem. Soc.* **1979**, *101*, 4586–4593.

(54) O'Sullivan, T.; Millar, M. M. *J. Am. Chem. Soc.* **1985**, *107*, 4096–4097.

Table 2. Spin Hamiltonian Energies

systems	relevant equations
$[Fe_2S_2(SR)_4]^{2-}$ $S_1 = S(Fe^{3+}) = {}^5/_2$ $S_2 = S(Fe^{3+}) = {}^5/_2$	$E(S) = [J_{ox}/2]S(S + 1)$ $\Longrightarrow \begin{cases} E(S_{max}) - E_B(ox) = ({}^{25}/_2)J_{ox} \\ E_B(ox) - E(S_{min}) = ({}^5/_2)J_{ox} \end{cases}$
$[Fe_2S_2(SR)_4]^{3-}$ $S_1 = S(Fe^{3+}) = {}^5/_2$ $S_2 = S(Fe^{2+}) = 2$	$E(S)_{g,u} = [J_{red}/2]S(S + 1) \pm B(S + {}^1/_2)$ $E(S)_{av(B)} = [J_{red}/2]S(S + 1)$ $\Longrightarrow \begin{cases} E(S_{max})_{av(B)} - E_B(red) = 10J_{red} \\ E_B(red) - E(S_{min})_{av(B)} = 2J_{red} \end{cases}$
$[Fe_4S_4(SR)_4]^{2-}$ $S_{12} = S(Fe^{2.5+} - Fe^{2.5+})$ $S_{34} = S(Fe^{2.5+} - Fe^{2.5+})$ $(S_{12})_{max} = (S_{34})_{max} = {}^9/_2$	$E(S) = [J_m/2]S(S + 1) \pm B(S_{12} + {}^1/_2) \pm B(S_{34} + {}^1/_2)$ $\Longrightarrow \begin{cases} E(S_{max}) - E_B(m) = ({}^{81}/_2)J_m \\ E_B(m) - E(S_{min}) = ({}^9/_2)J_m \end{cases}$
$[Fe_4S_4(SR)_4]^{3-}$ OC1($B' = 0$) and OC2($B' \neq 0$) $S_{12} = S(Fe^{2+} - Fe^{2+})$ $S_{34} = S(Fe^{2.5+} - Fe^{2.5+})$ $(S_{12})_{max} = 4$ $(S_{34})_{max} = {}^9/_2$	$E(S) = [J_{red}/2]S(S + 1) \pm B(S_{34} + {}^1/_2) \pm B'(S + {}^1/_2)$ $E(S)_{av(B')} = [J_{red}/2]S(S + 1) \pm B(S_{34} + {}^1/_2)$ $\Longrightarrow \begin{cases} E(S_{max})_{av(B')} - E_B(red) = 36J_{red} \\ E_B(red) - E(S_{min}) = 4J_{red} + B' \\ E_B(red) - E(S{=}{}^3/_2) = ({}^5/_2)J_{red} + 2B' \end{cases}$
$[Fe_4S_4(SR)_4]^{1-}$ OS3 $S_{12} = S(Fe^{3+} - Fe^{3+})$ $S_{34} = S(Fe^{2.5+} - Fe^{2.5+})$ $(S_{12})_{max} = 5$ $(S_{34})_{max} = {}^9/_2$	$E(S) = [J_{ox}/2]S(S + 1) \pm B(S_{34} + {}^1/_2) \pm B'(S + {}^1/_2)$ $E(S)_{av(B')} = [J_{ox}/2]S(S + 1) \pm B(S_{34} + {}^1/_2)$ $\Longrightarrow \begin{cases} E(S_{max})_{av(B')} - E_B(ox) = 45J_{ox} \\ E_B(ox) - E(S_{min})_{av(B')} = ({}^9/_2)J_{ox} \end{cases}$
$[Fe_4S_4(SR)_4]^{1-}$ OS1 and OS2 $S_{12} = S(Fe^{3+} - Fe^{3+})$ $S_{34} = S(Fe^{2.5+} - Fe^{2.5+})$ $(S_{12})_{max} = 4$ $(S_{34})_{max} = {}^9/_2$	$E(S) = [J_{ox}/2]S(S + 1) \pm B(S_{34} + {}^1/_2)$ $\Longrightarrow \begin{cases} E(S_{max}) - E_B(ox) = 36J_{ox} \\ E_B(ox) - E(S_{min}) = 4J_{ox} \end{cases}$

Table 2 and Figure 1a show the Heisenberg spin ladder, the effects of delocalization (resonance B term), and the positions of the high-spin and broken-symmetry states. We note that the resonance stabilization energy $B(S + {}^1/_2)$ is much smaller (by a factor of 5) for the $S_{min} = {}^1/_2$ ground state compared with the $S_{max} = {}^9/_2$ state. This energy, of the order of 0.1 eV in the low-spin ground state, can be readily quenched by vibronic effects, solvation effects, or other environmental influences. We will therefore neglect the B term for the reduced dimer ground state, and the associated redox potential calculation. This is also consistent with the usual observation of a trapped valence ground state by Mossbauer spectroscopy.

3.2. 4Fe4S Clusters. We now consider various 4Fe4S clusters. The 2- systems consist of four equivalent iron sites which we group in two mixed valence pairs with each iron oxidation state 2.5+. Each of these pairs is analogous to a 2Fe system in the reduced high-spin state, and this motivates the introduction of a delocalization term for each pair. Upon oxidation, we obtain the 1− systems with total spin $S = {}^1/_2$; Mossbauer spectroscopy of HIPIP complexes[55] shows that the four sites occur in two pairs, one of which is a mixed valence pair while the other one is formally composed of two ferric ions. Upon reduction of the 2− cluster form giving 3−, various spin states may be found. Usually, these sites appear at least in equivalent pairs.[56,57] These observations motivate us to write the spin Hamiltonian by grouping the irons into pairs and introducing various resonance terms (of non-Heisenberg form) to take into account pairwise delocalization as well as delocalization over the entire cluster. Such Hamiltonians have strong theoretical justification on first principles[58-60] and are quantitatively justified by the density functional results.[12] Depending on the oxidation state of the 4Fe cluster, 3 types of terms may be present in the spin Hamiltonian. The first is the Heisenberg term of the form

$$H = J\sum_{i<j}^{4} \hat{S}_i \cdot \hat{S}_j \tag{9}$$

which can be simplified for our purpose (we consider only energy differences between states having the same pair spin quantum numbers S_{12} and S_{34}) to

$$H = J\hat{S}_{12} \cdot \hat{S}_{34} \tag{10}$$

This last equation is like eq 7, but now coupling pair spins $S_{12} = S_1 + S_2$ and $S_{34} = S_3 + S_4$ instead of monomer spins. The pair spin S_{34} belongs to the mixed valence pair, while S_{12} belongs to a diferric, mixed valence, or diferrous pair depending on the cluster oxidation state (Table 2).

A broken-symmetry state and a corresponding high-spin state can be constructed from these pair spins. The pair spin quantum numbers used in the broken-symmetry energy equations must be maximal in a single J model.[12]

Further distinctions among the iron pairs, leading to a multi-J model, have been already discussed for the 1− species[61] as well as for 3− species[62,63] and will not be considered here in the calculation of redox potentials. Multi-J models can be quite important for issues of spin equilibria and spin crossover, but redox potentials are less sensitive to this.

The Heisenberg term acting alone displays a large degree of spin degeneracy, which is partially lifted by the introduction of resonance delocalization terms. This second type of term involves resonance delocalization within a mixed valence pair, of the form $\pm B(S_{ij} + {}^1/_2)$. There is one such pair for the 3− and 1− states, and two pairs for the 2− state of the 4Fe clusters. From the B terms, the lowest energy states obtained favor maximal pair spins for the mixed valence pairs. This *intralayer* resonance term is present in both high-spin and broken-symmetry states of each of the three 4Fe species presented here.

The third type of term describes possible resonance delocalization between the two distinct pairs composing the system (*interlayer* resonance), of the ferrous pair with the mixed valence pair (in the 3− cluster), and of the ferric pair with the mixed valence pair (in the 1− cluster). The contribution of this term to the spin Hamiltonian is of the form $\pm B'(S + {}^1/_2)$ involving the total spin S of the cluster. (We note that the magnitude of the B' parameter depends on the symmetry and character of the orbitals involved in *intralayer* resonance; consequently, for some electronic states, $B' = 0$ by symmetry, while for others $B' \neq 0$. Since the two energy roots of the B term $\pm B(S_{34} + {}^1/_2)$ also differ in symmetry, the magnitude of B' is also dependent on the sign of the root taken.) By analogy with the reduced dimer case, we define an average state $E(S)_{av(B')}$ where the B' resonance term is averaged out (quenched) but the B term is kept. Such an averaging process is needed to evaluate the spin coupling constants (see Table 2). Moreover, in the case of the oxidized HiPIP system, with B' being of the order of 300 cm^{-1}, the

---

(55) Papaefthymiou, V.; Millar, M. M.; Münck, E. *Inorg. Chem.* **1986**, *25*, 3010–3014.

(56) Carney, M. J.; Papaefthymiou, G. C.; Spartalian, K.; Frankel, R. B.; Holm, R. H. *J. Am. Chem. Soc.* **1988**, *110*, 6084–6095.

(57) Auric, P.; Gaillard, J.; Meyer, J.; Moulis, J. M. *Biochem. J.* **1987**, *242*, 525–530.

(58) Blondin, G.; Girerd, J. J. *Chem. Rev.* **1990**, *90*, 1359–1376.

(59) Papaefthymiou, V.; Girerd, J. J.; Moura, I.; Moura, J. J. G.; Münck, E. *J. Am. Chem. Soc.* **1987**, *109*, 4703–4710.

(60) Anderson, P. W.; Hasegawa, H. *Phys. Rev.* **1955**, *100*, 675–681.

(61) Noodleman, L. *Inorg. Chem.* **1988**, *27*, 3677–3679.

(62) Noodleman, L. *Inorg. Chem.* **1991**, *30*, 246–256.

(63) Noodleman, L. *Inorg. Chem.* **1991**, *30*, 256–264.

Table 3. Spin Hamiltonian Parameters[a]

system	state	geometry	J	B'	B	J_{red}/J_{ox}	B/J	B'/J
$[Fe_2S^*_2(SCH_3)_4]^{2-}$	oxidized	D_{2h}	763					
$[Fe_2S^*_2(SCH_3)_4]^{3-}$	reduced	C_{2v}	514		394	0.90	0.60	
$[Fe_4S^*_4(SCH_3)_4]^{3-}$	OC1	D_{2d}	559	0	712	0.87	1.27	0
		"relaxed"	467	0	695	0.72	1.49	0
	OC2	D_{2d}	629	588	779	0.98	1.24	0.93
		"relaxed"	519	618	753	0.80	1.45	1.19
$[Fe_4S^*_4(SCH_3)_4]^{2-}$	REF	D_{2d}	645		795		1.23	
$[Fe_4S^*_4(SCH_3)_4]^{1-}$	OS1	D_{2d}	691	0	832	0.93	1.20	0
	a	C_{2v}	725	~0	933	0.89	1.29	~0
	b		726	~0	976	0.89	1.34	~0
	OS2	D_{2d}	637	0	824	1.01	1.29	0
	a	C_{2v}	657	~0	887	0.98	1.35	~0
	b		663	~0	936	0.97	1.41	~0
	OS3	D_{2d}	685	289	787	0.94	1.15	0.42
	a	C_{2v}	712	281	866	0.91	1.20	0.39
	b		723	281	925	0.89	1.28	0.39

[a] Values in cm^{-1}.

interlayer delocalization is usually quenched due to vibrational or solvent trapping for the spin ground state which is therefore of the form $E(S_{min} = {}^1/_2)_{av(B')}$. Finally we note that the calculated broken-symmetry state is *pairwise* delocalized by construction (B' term quenched) rather than *fully* delocalized. We use the solvation energy calculated for the broken-symmetry state as a reasonable approximation to the solvation energy of the pairwise delocalized pure-spin state $E(S = {}^1/_2)_{av(B')}$, since we cannot directly calculate the electron density of this pure-spin state within density functional theory.

The spin equilibria described so far are for states in vacuum without solvation. In the presence of solvent, the spin states with energies $E(S)_{av(B')}$ (*pairwise delocalized*) and $E(S)$ (*fully* delocalized over the cluster) will not have the same solvation energies. We expect more stabilization from solvation for the pairwise delocalized states, since these have net molecular dipole moments, whereas the fully delocalized states have an extra energetic gain through the B' resonance term, but less favorable solvation energies. An intermediate stage of delocalization between pairwise and fully delocalized is also possible.[12,58] Consequently, the relative stabilization is clearly a matter of competition between solvation energy and interlayer delocalization. This competition will favor fully delocalized states for large S, even in the presence of solvent, but pairwise delocalization becomes more favored for small S. Since the Heisenberg part of the Hamiltonian also generally favors small S, it is not surprising that ground spin states for the reduced 4Fe cluster with $S = {}^3/_2$ have been observed, which are either fully or pairwise delocalized (or possibly intermediate in character). Further, nearly degenerate $S = {}^1/_2, {}^3/_2$ ground states have been found, and there is also strong evidence for quantum spin-admixed $S = {}^1/_2, {}^3/_2$ states in several cases.[2,13,56,64]

3.3. Barycenters of Spin Coupling and Electron Delocalization. The energies of the ground spin states, as well as those of the broken-symmetry and high-spin states, all intrinsically contain Heisenberg spin coupling as well as electron delocalization terms. It is valuable to construct spin and delocalization barycenter energies, where spin coupling and electron delocalization effects have been averaged out. These are analogous to the center of gravity (barycenter) energy for ligand field splittings, but now represent the degeneracy weighted average, equivalently, the "noninteracting" or "uncoupled" state with respect to Heisenberg spin coupling or electron delocalization. The energy difference between the barycenter and the ground state can then be interpreted as the energy stabilization due to "turning on" the coupling effects. These energy differences will be called ΔE_{BAR-J} (Heisenberg spin coupling contribution) ΔE_{BAR-B} (electron delocalization effects). In this section, only pairwise delocalization terms will be treated, and B' terms will always be averaged out. The whole stabilization energy of the ground state GS relative to the barycenter state E_{BAR} is then $\Delta E_{BAR} = E_{BAR} - E(GS) = \Delta E_{BAR-J} + \Delta E_{BAR-B}$.

Once fixed site spin and S_{12}, S_{34} pair spin values are constructed, it is straightforward to develop the corresponding spin (or delocalization) barycenter energy for any state of the 4Fe4S systems, and similar considerations apply to the 2Fe2S systems with fixed S_1, S_2. We are interested principally in the specific S_{12}, S_{34} values associated with the lowest energy state for each oxidation level, and these will then be used to generate the spin ladder $|S_{34}S_{12}S\rangle$ for the corresponding spin barycenter equation. The choice of $S_{12} = S_{34} = {}^9/_2$ for 2−, and of $S_{12} = 4$, $S_{34} = {}^9/_2$ for 3−,1−, is based on likely states as found from our calculations, and phenomenological analysis of experimental data.[12,61,65,66] The equations presented in Table 4 were evaluated for these pair spin quantum numbers. Other selections of pair spins could also be made: for example, $|{}^7/_2\ 3\ {}^1/_2\rangle$ is the expected ground state for the 1− cluster in some cases,[65,66] and one could generate a spin barycenter energy for the ladder $|{}^7/_2\ 3\ S\rangle$. The spin barycenter energy differences for this will differ significantly from those generated for the ladder $|{}^9/_2\ 4\ S\rangle$. This affects the decomposition of the redox potential, but has a much smaller effect on the final calculated redox potential, as will be shown in the next section.

For Heisenberg spin coupling, let the energy of a spin state be $E(S) = (J/2)S(S + 1)$ with degeneracy $D(S) = 2S + 1$. Then the spin barycenter energy difference is

$$\Delta E_{BAR-J} = \left[\sum_{S=S_{min}}^{S=S_{max}} D(S)E(S) / \sum_{S=S_{min}}^{S=S_{max}} D(S) \right] - E(S_{min}) \qquad (11)$$

where it is convenient to reference the energies $E(S)$ to the corresponding $E(S_{min})$. Using the algebra of finite series, we calculated ΔE_{BAR-J} for 2Fe2S and 4Fe4S systems in their different oxidation states. (See Table 4 for the expressions and Figure 1 for the relative position of the spin barycenter energy E_{BAR} with respect to the Heisenberg ladder in the case of the reduced 2Fe2S dimer and oxidized 4Fe4S tetramer.)

To include electron delocalization from the B term in the barycenter description, we note that the resonance delocalization energy within a mixed valence pair is $\pm B(S_{ij} + {}^1/_2)$, with $S_{ij} =$

---

(64) Carney, M. J.; Papaefthymiou, G. C.; Whitener, M. A.; Spartalian, K.; Frankel, R. B.; Holm, R. H. *Inorg. Chem.* **1988**, *27*, 346–352.

(65) Jordanov, J.; Roth, E. K. H.; Fries, P. H.; Noodleman, L. *Inorg. Chem.* **1990**, *29*, 4288–4292.

(66) Mouesca, J.-M.; Rius, G.; Lamotte, B. *J. Am. Chem. Soc.* **1993**, *115*, 4714–4731.

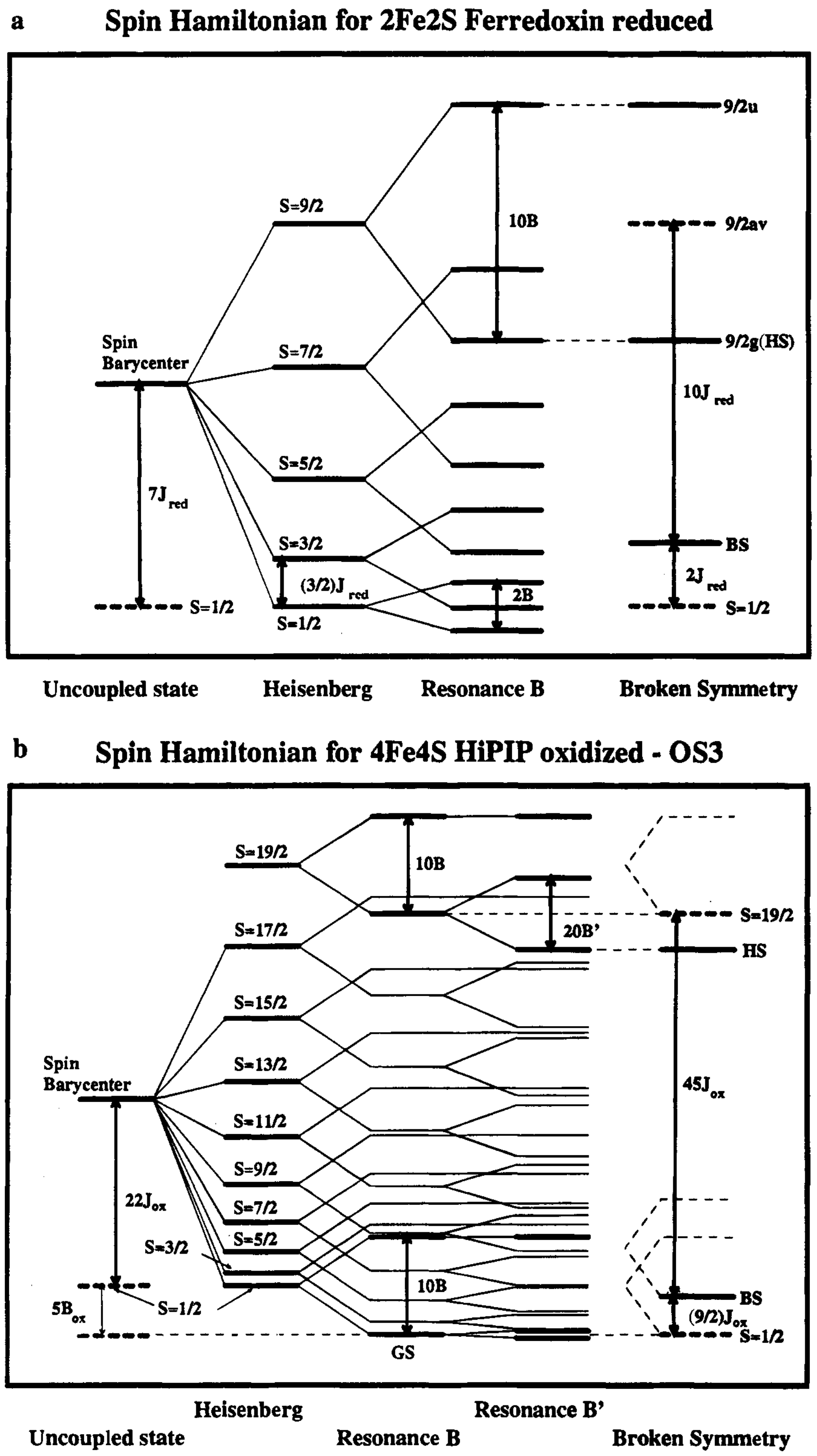

Figure 1. (a) Spin state energy diagram for reduced $[Fe_2S_2(SR)_4]^{3-}$, R = CH_3: (left) Positions of spin barycenter energy (E_{BAR}) and spin ground state ($S = {}^1/_2$); (middle) Heisenberg spin ladder + resonance splitting (the resonance splitting in the high spin $S = {}^9/_2$ state is indicated); (right) calculated broken symmetry (BS), and lowest energy high spin (HS) states (thick lines). The energy difference $10J_{red}$ is shown by the arrows. From this, the energy difference $2J_{red}$ between BS and ground state ($S = {}^1/_2$) is determined. (b) Spin states of oxidized high potential $[Fe_4S_4(SR)_4]^{1-}$, electronic state, OS3: (left) the spin barycenter energy is shown relative to the Heisenberg only ground state ($S = {}^1/_2$), and including the effect of *intralayer* resonance ($5B_{ox}$) in the ground state GS; (middle) Heisenberg spin ladder, plus effect of *intralayer* resonance delocalization (B), adding the effect of *interlayer* resonance (B'); (right) calculated broken symmetry (BS), and lowest high spin (HS) state. The calculated Heisenberg energy difference $45J_{ox}$ is shown. The position of GS is determined by subtracting $({}^9/_2)J_{ox}$ from the BS energy.

$S_{34} = {}^9/_2$ for the delocalized pair in the 3−,1− clusters, while $S_{12} = S_{34} = {}^9/_2$ for the two delocalized pairs in the 2− cluster. This contributes to a further stabilization of the ground state by ΔE_{BAR-B} (with respect to $E(S_{min})$ deduced from Heisenberg interactions only) of $5B$ per mixed valence pair.

Finally, the redox potential E° for a given redox couple can be decomposed into a sum

$$E^\circ = \mathrm{IP(red)} + \Delta E_{PB} + \Delta(\mathrm{SHE}) \qquad (12)$$

with

$$\mathrm{IP(red)} = E^{\mathrm{ox}}(\mathrm{GS}) - E^{\mathrm{red}}(\mathrm{GS})$$

$$= [E^{\mathrm{ox}}_{\mathrm{BAR}} - \Delta E^{\mathrm{ox}}_{\mathrm{BAR}}] - [E^{\mathrm{red}}_{\mathrm{BAR}} - \Delta E^{\mathrm{red}}_{\mathrm{BAR}}]$$

$$= [E^{\mathrm{ox}}_{\mathrm{BAR}} - E^{\mathrm{red}}_{\mathrm{BAR}}] + [\Delta E^{\mathrm{red}}_{\mathrm{BAR}_{-J}} - \Delta E^{\mathrm{ox}}_{\mathrm{BAR}-J}] + [\Delta E^{\mathrm{red}}_{\mathrm{BAR}-B} - \Delta E^{\mathrm{ox}}_{\mathrm{BAR}-B}]$$

$$= \mathrm{IP(red)}_{\mathrm{un}} + \Delta JT + \Delta BT \qquad (13)$$

and therefore

$$E^\circ = [\mathrm{IP(red)}_{\mathrm{un}} + \Delta E_{\mathrm{PB}} + \Delta(\mathrm{SHE})] + \Delta JT + \Delta BT$$

$$= E^\circ_{\mathrm{un}} + \Delta JT + \Delta BT \qquad (14)$$

Here $\mathrm{IP(red)_{un}}$ and E°_{un} are the uncoupled reduced state ionization potential and uncoupled redox potential. The theoretical expressions for the terms ΔJT (contribution to the redox potential of the Heisenberg spin coupling) and ΔBT (contribution to the redox potential of the resonance delocalization) are given in Table 4. This decomposition will prove useful in understanding variations in redox potentials with changes in cluster size and charges of the redox couple.

4. Results and Discussion

4.1. Oxidized High Potential [4Fe4S] Electronic and Spin States. For the oxidized high potential (1−) form of the cluster, we have found three low lying electronic orbital configurations, which we shall denote OS1, OS2, and OS3. Figure 2 shows the energy level diagram for the highest occupied and lowest unoccupied orbitals of the simplest of these, OS3. Since the coordinate system, the symmetry, and the Fe−Fe axis labeling are interrelated, let the two Fe−Fe pairs be $\mathrm{Fe_a{-}Fe_a}$ (x axis) and $\mathrm{Fe_b{-}Fe_b}$ (y axis) with associated layers $[\mathrm{Fe_2S^*_2(SR)_2}]_{\mathrm{a,b}}$ for "layer a,b" respectively. There are two intralayer and four interlayer Fe−Fe bonds. Starting from $\mathrm{HP_{red}}$, we remove one electron from σ bonding $\mathrm{Fe_{1a}(d_{x^2-y^2}) + Fe_{2a}(d_{x^2-y^2})}$ orbital $20\mathrm{A_1}\beta$ (layer a), producing a hole there, and making the $\mathrm{Fe_a{-}Fe_a}$ pair the $\mathrm{Fe^{3+}{-}Fe^{3+}}$ pair. The $\mathrm{Fe_b{-}Fe_b}$ pair remains the delocalized mixed valence pair $\mathrm{Fe^{2+}{-}Fe^{3+}}$. This gives the state 4Fe, 1−, OS3, shown in Figure 2. The state OS1 is obtained from OS3 by the spin forbidden transition $14\mathrm{B_1}\alpha$(layer a) → $20\mathrm{A_1}\beta$(layer a). The $14\mathrm{B_1}\alpha$(layer a) orbital is largely a mixture of $\mathrm{Fe_a(d_{x^2-y^2})}(19\%) + \mathrm{Fe_a(d_{z^2})}(11\%) + (\mathrm{S^*_a})(\mathrm{p}_x)(25\%) + \mathrm{S_a}(\mathrm{p}_x)(12\%)$. It then has the character of a spin forbidden mixed Fe d → d and S,S* → Fe d charge transfer transition. The state OS2 is similarly obtained by the spin forbidden $13\mathrm{B_2}\alpha$(layer a) → $20\mathrm{A_1}\beta$(layer a) transition. The composition of $13\mathrm{B_2}\alpha$ is about $\mathrm{Fe_a(d_{xy})}(26\%) + \mathrm{S_a}(\mathrm{p}_y)(33\%) + \mathrm{S^*_a}(\mathrm{p}_y)(16\%)$. The density functional calculations show that all three states should lie within about 0.3 eV of each other in vacuum for D_{2d} geometry, with OS1 lying lowest.

Some subtle issues exist involving both spin equilibria and electronic orbital states. The spin algebra for OS1 and OS2 is identical so these need only to be distinguished from OS3. Since in previous work[61] OS3 was assumed to be the ground state of oxidized high potential $\mathrm{HP_{ox}}$ clusters and proteins, new possibilities are now open for a better understanding of the variety of physics present in these clusters.

A separate spin ladder will exist for each low lying electronic state, and we now need to examine the site and pair spin quantum numbers likely for these systems. We begin with the orbital state OS3.[61] With each $\mathrm{Fe^{3+}}$ ion as high spin, $S_1 = S_2 = {}^5/_2$, and with high-spin sites for the mixed valence pair, possible pair spin quantum numbers are $0 \le S_{12} \le 5$, and ${}^1/_2 \le S_{34} \le {}^9/_2$. In a single-$J$ model, the lowest energy states have $S_{34} = {}^9/_2$ (maximum), $S_{12} = 4$ or 5 (degenerate), and $S = {}^1/_2$ (minimum), assuming antiferromagnetic Heisenberg coupling, and a substantial B term.[61]

Table 4. Spin Barycenter Energy Differences

system	heisenberg	resonance
$[\mathrm{Fe_2S_2(SR)_4}]^{2-}$	$\Delta E^{\mathrm{ox}}_{\mathrm{BAR}\text{-}J} = 9J_{\mathrm{ox}}$	$\Delta E^{\mathrm{ox}}_{\mathrm{BAR}\text{-}B} = 0$
$[\mathrm{Fe_2S_2(SR)_4}]^{3-}$	$\Delta E^{\mathrm{red}}_{\mathrm{BAR}\text{-}J} = 7J_{\mathrm{red}}$	$\Delta E^{\mathrm{red}}_{\mathrm{BAR}\text{-}B} = 0$
$[\mathrm{Fe_2S_2(SR)_4}]^{2-/3-}$	$\Delta JT = 7J_{\mathrm{red}} - 9J_{\mathrm{ox}}$	$\Delta BT = 0$
$[\mathrm{Fe_4S_4(SR)_4}]^{1-}$	$\Delta E^{\mathrm{ox}}_{\mathrm{BAR}\text{-}J} = 22J_{\mathrm{ox}}$	$\Delta E^{\mathrm{ox}}_{\mathrm{BAR}\text{-}B} = 5B_{\mathrm{ox}}$
$[\mathrm{Fe_4S_4(SR)_4}]^{2-}$	$\Delta E^{\mathrm{m}}_{\mathrm{BAR}\text{-}J} = 25J_{\mathrm{m}}$	$\Delta E^{\mathrm{m}}_{\mathrm{BAR}\text{-}B} = 10B_{\mathrm{m}}$
$[\mathrm{Fe_4S_4(SR)_4}]^{3-}$	$\Delta E^{\mathrm{red}}_{\mathrm{BAR}\text{-}J} = 22J_{\mathrm{red}}$	$\Delta E^{\mathrm{red}}_{\mathrm{BAR}\text{-}B} = 5B_{\mathrm{red}}$
$[\mathrm{Fe_4S_4(SR)_4}]^{1-/2-}$	$\Delta JT = 25J_{\mathrm{m}} - 22J_{\mathrm{ox}}$	$\Delta BT = 10B_{\mathrm{m}} - 5B_{\mathrm{ox}}$
$[\mathrm{Fe_4S_4(SR)_4}]^{2-/3-}$	$\Delta JT = 22J_{\mathrm{red}} - 25J_{\mathrm{m}}$	$\Delta BT = 5B_{\mathrm{red}} - 10B_{\mathrm{m}}$

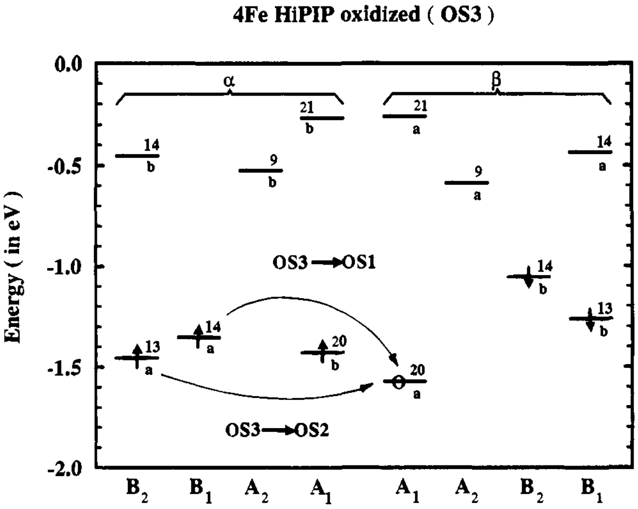

Figure 2. Energy levels for highest occupied and lowest unoccupied orbitals of $[\mathrm{Fe_4S_4(SR)_4}]^{1-}$ $\mathrm{HP_{ox}}$, electronic state OS3. Spin forbidden transitions giving states OS1 and OS2 are indicated. Spin-up arrows indicate occupied α spin orbitals, down-spin arrows occupied β spin orbitals. The empty hole (O) is β (down) spin. Small a and b indicate the $\mathrm{Fe_2S^*_2(SR)_2}$ layer a or b involved for that orbital. Layer a corresponds to the high spin differic pair, while layer b contains the delocalized mixed valence iron pair. The formal spin population is obtained from this by adding 8e⁻ (α spin) to layer a and 8e⁻ (β spin) to layer b from deeper lying orbitals.

The antiferromagnetic (AF) coupling of a $2\mathrm{Fe^{3+}}$ dimer is expected to be larger than the other Heisenberg AF couplings in the system. If the J_{12} parameter of the ferric pair is distinguished from the J coupling between sites of the mixed valence and ferric pairs by $J_{12} = J + \Delta J_{12}$, then the degeneracy between states with $S_{12} = 4$ *or* 5 is lifted, and the energy difference between $|{}^9/_2\ 5\ {}^1/_2\rangle$ and $|{}^9/_2\ 4\ {}^1/_2\rangle$ is $5\Delta J_{12}$.[61] On the basis of the phenomenological fits to magnetic data,[65] ΔJ_{12} is about 150 cm⁻¹, which would give a contribution of only about 0.1 eV to the redox potential. For reasonable spin coupling parameter values $|{}^7/_2\ 3\ {}^1/_2\rangle$ is also a likely ground state.[55,61,65,66] This is consistent also with observed ^{57}Fe hyperfine spectra by ENDOR and Mossbauer spectroscopies and with magnetic susceptibility data.[55,65,66] Further, Mossbauer observations require that the mixed valence pair spins be aligned with the system spin and that the ferric pair spins be oppositely aligned so $S_{34} > S_{12}$.[55,61,65,66] We note also that the ferric pair spin quantum numbers $S_{12} = 3$, 4 represent "canting" of the ferric pair spins compared to the maximum value $S_{12} = 5$ (for two high-spin $S_1 = S_2 = {}^5/_2$ sites) while $S_{34} = {}^7/_2$ is "canted" compared to $S_{34} = {}^9/_2$.

The spin barycenter equations depend only on the pair spins and the total spin of the ground state. Thus the spin barycenter equations are identical for OS1, OS2, and OS3 with $|^9/_2\ 4\ ^1/_2\rangle$ as the ground state (Table 4). By contrast, if the ground state is "canted" with spins $|^7/_2\ 3\ ^1/_2\rangle$, the value of $\Delta E^{\text{ox}}_{\text{BAR}-J} = 13.5J_{\text{ox}}$, and $\Delta E^{\text{ox}}_{\text{BAR}-B} = 4B_{\text{ox}}$. This will significantly alter the ΔJT and slightly alter the ΔBT terms. In contrast with the expected pure spin ground state, there is no "spin canting" for the broken symmetry state, which is obtained by opposite alignment of the $\vec{S}_{12}$ and $\vec{S}_{34}$ spin vectors. By construction, both of these must have maximal spin, giving $S_{12} = 5$, $S_{34} = ^9/_2$ for OS3.

The net effect of this additional spin canting on the ground state and the redox potential can be treated within the same framework. The energy difference between $|^7/_2\ 3\ ^1/_2\rangle$ and $|^9/_2\ 4\ ^1/_2\rangle$ is $-4\Delta J_{12} + B$; either of these states may be the ground state, but the effect on the redox potential will be small for typical values of these parameters. The decomposition of the redox potential into $\overset{\circ}{E}_{\text{un}}$, ΔJT, and ΔBT terms will be changed; however, the net effect is that the ΔJT term becomes more positive by about 0.7 eV, ΔBT more positive by about 0.1 eV, but $\overset{\circ}{E}_{\text{un}}$ becomes more negative by an amount nearly equal to $\Delta BT + \Delta JT$ (see eqs 12 to 14).

To summarize the argument above, the principal broken symmetry state is constructed using maximal pair spins of $S_{12} = 5$, and $S_{34} = ^9/_2$; the physical states are expected to arise from "spin canting" of the high spin ferric sites, with possible additional spin canting of both S_{12}, S_{34} yielding lower spin quantum numbers. ($S_{12} = 3$, $S_{34} = ^7/_2$ represents about the lowest values possible consistent with ENDOR and Mossbauer spectroscopy.) This is the construction followed for the orbital electronic state called OS3, and its associated broken-symmetry state.

Alternative orbital electronic states can be constructed, however, where the ferric pair contains a mixture of $S_1 = ^3/_2$, $S_2 = ^5/_2$ sites (along with the permutation $S_1 = ^5/_2$; $S_2 = ^3/_2$). To see this, we start with the principal broken-symmetry state $S_{12} = 5$, $S_{34} = ^9/_2$ above, and make a spin-forbidden transition within the S_{12} pair. Both bridging and terminal sulfur ligands as well as Fe sites are involved in the transition. Then in place of net $10\alpha,0\beta$ electrons for $S_{12} = 5$, $M_{S12} = 5$, we have $9\alpha1\beta$ electrons so that $S_{12} = 4$, $M_{S12} = 4$. Clearly, such a result cannot represent parallel alignment of high-spin 2Fe^{3+} sites, but it can represent parallel alignment of a mixture of high and intermediate spin S_1,S_2 = $^5/_2$,$^3/_2$ sites; spin-forbidden charge transfer excitations from $S,S^* \rightarrow 2\text{Fe}^{3+}$ may also contribute here. The states OS1 and OS2 are of this character. The spin algebra of these two electronic states is formally equivalent to those of the reduced cluster, since $S_{12} = (n - 2)/2 = 4$, $S_{34} = ^9/_2$, $S_{\min} = ^1/_2$, $S_{\max} = ^{17}/_2$ (Table 2).

4.2. Electronic States of Reduced 4Fe4S Clusters. For reduced 4Fe clusters, we found in earlier work that there are two likely orbital configurations,[42] which here we call OC1 and OC2 (see Figure 3).[12] These are obtained from the oxidized state 4Fe, 2− by adding one electron either to $14\text{B}_1\beta$ or $9\text{A}_2\beta$ (layer a, minority spin). Fe_a−Fe_a now becomes the Fe^{2+}−Fe^{2+} pair, and Fe_b−Fe_b the delocalized mixed valence pair. The orbital $14\text{B}_1\beta$ (layer a) is σ^*, the antibonding $\text{Fe}_{1a}(d_{x^2-y^2})$−$\text{Fe}_{2a}(d_{x^2-y^2})$ counterpart to the occupied σ bonding level $20\text{A}_1\beta$ (layer a). By contrast, $9\text{A}_2\beta$ (layer a) is a δ^* orbital, mainly of the form $\text{Fe}_{1a}(d_{yz})$−$\text{Fe}_{2a}(d_{yz})$. In previous work,[12,42] we have discussed both the expected differences in Mossbauer properties of these two states (OC1 should have a larger quadrupole splitting for the ferrous pair than OC2); and spin equilibria OC1 can have only an $S = ^1/_2$ ground state, while either $S = ^1/_2$ or $S = ^3/_2$ is feasible for OC2.

4.3. ESP and Mulliken Charges. In Tables 5 and 6 we present results for ESP charges of the broken symmetry states, along with the corresponding spin populations of the 1Fe, 2Fe, and 4Fe systems. The geometries for all clusters were taken from Table 1; for the $[\text{Fe}_4\text{S}_4(\text{SR})_4]^{2-,1-}$ clusters, we report the Holm (D_{2d}) geometry results, while for the $[\text{Fe}_4\text{S}_4(\text{SR})_4]^{3-}$, we report the relaxed geometry, since these give the lowest state energies from those geometries tested. ESP charges depend only weakly on these small variations in geometry. Spin populations were determined by a Mulliken analysis, since there is no simple way to partition spin populations analogous to an ESP charge decomposition. Table 6 gives Mulliken charges for comparison with ESP charges in the 4Fe systems.

For all the clusters examined, the ESP charge analysis gives the surprising result that the iron atoms become effectively more positive as the clusters are reduced, while all the sulfurs become substantially more negative. All sulfur sites exhibit roughly similar charge shifts upon reduction in the 4Fe and 2Fe complexes. The absolute magnitudes of these ESP charges are larger than those from the Mulliken analysis, so that the corresponding polarity of all the Fe−S bonds is higher within the ESP framework. These observations contrast strongly with the behavior expected simply from the changes in formal Fe oxidation state, from $\text{Fe}^{3+} \rightarrow \text{Fe}^{2+}$ in 1Fe and 2Fe clusters, and from $\text{Fe}^{3+} \rightarrow \text{Fe}^{2.5+}$, $\text{Fe}^{2.5+} \rightarrow \text{Fe}^{2+}$ in 4Fe clusters. Evidently, the effects of electron relaxation upon reduction are large;

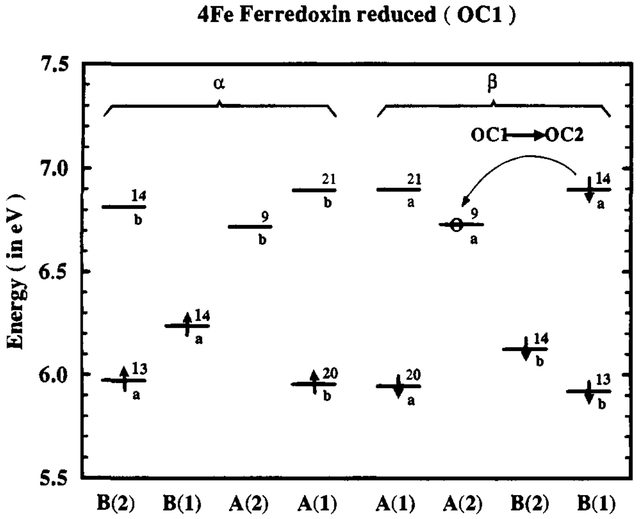

Figure 3. Energy levels for highest occupied and lowest unoccupied orbitals of $[\text{Fe}_4\text{S}_4(\text{SR})_4]^{3-}$, Fd_{red}, electronic state OC1. The spin allowed transition giving state OC2 is indicated. Layer a contains the high spin differous pair, while layer b contains the delocalized mixed valence pair.

Table 5. Charges and Spin Populations for 1Fe and 2Fe Systems

$[\text{Fe(SCH}_3)_4]^{2-/1-}$

	ESP charges		spin populations	
atom	2−	1−	2−	1−
Fe	+0.900	+0.813	+3.338	+3.577
S	−0.708	−0.507	+0.159	+0.326
CH_3	−0.017	+0.054	+0.006	+0.032

$[\text{Fe}_2\text{S*}_2(\text{SCH}_3)_4]^{3-/2-}$

	ESP charges		spin populations	
atom	3−	2−	3−	2−
Fe_{ox}	+0.907	+0.761	+3.256	+3.119
Fe_{red}	+0.818	+0.761	−2.847	−3.119
S*	−0.780	−0.614	+0.174	0.000
S_{ox}	−0.731	−0.590	+0.187	+0.235
S_{red}	−0.804	−0.590	−0.100	−0.235
$\text{CH}_{3\text{ox}}$	−0.013	+0.015	+0.028	+0.026
$\text{CH}_{3\text{red}}$	−0.034	+0.015	+0.007	−0.026

Table 6. Charges and Spin Populations for $[Fe_4S^*_4(SCH_3)_4]^{3-,2-,1-}$

	3−		2−	1−		
atom	OC1	OC2	REF	OS1	OS2	OS3
A. ESP Charges						
Fe_{ox}	+0.518	+0.484	+0.409	+0.304	+0.286	+0.343
Fe_{red}	+0.460	+0.481	+0.409	+0.321	+0.340	+0.326
S^*_{ox}	−0.576	−0.542	−0.393	−0.233	−0.232	−0.249
S^*_{red}	−0.513	−0.523	−0.393	−0.238	−0.267	−0.260
S_{ox}	−0.716	−0.710	−0.567	−0.398	−0.383	−0.416
S_{red}	−0.707	−0.724	−0.567	−0.429	−0.416	−0.419
CH_{3ox}	+0.028	+0.020	+0.050	+0.084	+0.089	+0.086
CH_{3red}	+0.007	+0.014	+0.050	+0.089	+0.085	+0.090
B. Mulliken Charges						
Fe_{ox}	+0.087	+0.089	+0.021	−0.044	−0.034	+0.009
Fe_{red}	+0.071	+0.070	+0.021	−0.016	−0.011	−0.011
S^*_{ox}	−0.354	−0.346	−0.206	−0.080	−0.093	−0.119
S^*_{red}	−0.323	−0.322	−0.206	−0.081	−0.100	−0.097
S_{ox}	−0.329	−0.331	−0.211	−0.082	−0.071	−0.093
S_{red}	−0.325	−0.338	−0.211	−0.100	−0.103	−0.096
CH_{3ox}	−0.157	−0.158	−0.105	−0.047	−0.043	−0.044
CH_{3red}	−0.169	−0.163	−0.105	−0.050	−0.046	−0.049
C. Spin Populations						
Fe_{ox}	+2.886	+2.835	+2.668	+2.086	+2.130	+2.858
Fe_{red}	−2.550	−2.472	−2.668	−2.502	−2.513	−2.541
S^*_{ox}	+0.186	+0.120	−0.001	−0.090	−0.066	+0.077
S^*_{red}	−0.049	−0.026	+0.001	−0.006	+0.055	+0.049
S_{ox}	+0.140	+0.137	+0.185	+0.209	+0.130	+0.285
S_{red}	−0.125	−0.092	−0.185	−0.200	−0.226	−0.232
CH_{3ox}	+0.010	+0.010	+0.014	+0.019	+0.014	+0.022
CH_{3red}	+0.001	−0.013	−0.014	−0.015	−0.021	−0.019

electron relaxation in the passive orbitals exceeds the change in electron density in the active orbital of the redox process; the active orbital is of mainly Fe character in all cases except OS1 and OS2 of 4Fe, 1− (HP_{ox}).

Table 7 gives a comparison of the solvation energy difference terms calculated with Mulliken versus ESP charges. Surprisingly, despite a significant difference in the charges obtained from a Mulliken versus ESP procedure, the predicted values of ΔE_{PB} are similar, with differences of at most 0.12 eV. While individual solvation energies can vary by up to 0.2 eV, usually with greater solvation for the ESP than for Mulliken charges, these differences partially cancel in the solvation energy difference ΔE_{PB}; similarly, atomic charge differences (red−ox) vary much less than absolute atomic charges when Mulliken and ESP procedures are compared. In these highly charged systems, total charges and molecular size and shape evidently have a larger effect on ΔE_{PB} than does Fe−S bond polarity.

In the initial stages of our work, we also compared redox potentials calculated using the VSB potential with those using an Xα potential for 4Fe complexes. These early calculations used Mulliken charges. We found that the solvation energy differences ΔE_{PB} were very close (within about 0.02 eV) comparing VSB with Xα for either the 3−/2− or 2−/1− couples. The electronic IP(red) term is somewhat more negative with an Xα compared to a VSB potential, by −0.18 eV for 3−/2− and −0.12 eV for 2−/1−, so that the VSB results give slightly better agreement with experiment. Overall, it is surprising that the two different exchange-correlation potentials give redox potentials that are so similar. (Significant differences in J parameters are found comparing Xα and VSB potentials, with smaller J values for Xα, while there are much smaller differences for B, B'; one can compare Table 3 with Table 1 of ref 12. However, even these differences in J parameters contribute only −0.09 eV to the redox potential difference for 3−/2−, and −0.01 eV to that for 2−/1−; this energy term is of the form $\Delta(\Delta JT)$ and is part of the IP(red) difference above.)

We have previously calculated charge distributions in 1Fe, 2Fe, and 4Fe complexes using the Xα scattered wave method (Xα−SW).[42,67] This method differs from VSB-LCAO both in the exchange-correction potential used, and in the analytic/numerical methods used to solve the self-consistent field equations.[68] Further, the SW model uses a partitioning method to determine atomic charges, based on the electron distribution in different regions of space.[69] We can then compare the atomic charges and charge differences upon reduction (red-ox) of the earlier calculations with our present ESP and Mulliken results. The Xα-SW charges show considerably less bond polarity than the ESP charges, and comparable polarity to Mulliken charges. Upon reduction, most of the increase in negative charge goes to the S,S* atoms for all FeS clusters considered, just as found with ESP or Mulliken charge differences. Unlike the ESP and Mulliken charge differences, however, the Xα-SW charges on Fe do not become more positive on reduction, and the changes in negative charge on S,S* are typically smaller, about 70% of that found with the ESP or Mulliken calculations.

4.4. Spin Populations. The Mulliken spin populations (Tables 5 and 6) behave mainly as expected: in nearly all cases, the magnitude of the Fe spin population decreases upon reduction of the corresponding site, so that there is monotonic decrease in spin population for a given cluster as the formal site oxidation state is reduced from $Fe^{3+} \rightarrow Fe^{2.5+} \rightarrow Fe^{2+}$. We note, however, the unusual behavior of states OS1 and OS2 of the oxidized HP cluster. For example, the spin population of the 4Fe,2− cluster sites with formal oxidation state $2Fe^{2.5+}$ (2.67) is substantially higher than those of OS1 and OS2, with formal oxidation state $2Fe^{3+}$ (2.09, 2.13). This is clearly due to the intermediate site spin character of the diferric sites, $S_1,S_2 = {}^3/_2, {}^5/_2, S_{12} = 4$; by contrast, the spin population of each of the diferric sites of OS3 (2.86) is greater than that in the mixed valence sites of 4Fe,2−. We note also that the spin populations on the terminal S_{ox} sites are smaller in OS1 and OS2 than in OS3. Also, the sign of the spin population on the bridging S^*_{ox} sites is opposite to that on Fe_{ox} in OS1 and OS2 but these have the same sign in OS3. This happens because OS1 and OS2 can be obtained from OS3 by single spin forbidden transitions, which are a mixture of spin forbidden S,S* → Fe(ox) and Fe(ox)d → d type. Overall, considerable Fe−S covalency is apparent in the metal site spin populations, since the calculated spin populations are considerably less than the idealized values of 5, 4.5, and 4 respectively for the formal oxidation states Fe^{3+}, $Fe^{2.5+}$, and Fe^{2+}. One measure of metal−ligand covalency is the ratio of the actual to the formal site spin population (spin population ratio), so lower percentages represent greater covalency. The spin population ratio by this criteria ranges from about 42% (OS1 and OS2 Fe_{ox}) and about 60% (otherwise) for 4Fe4S, to about 65 to 70% for 2Fe2S, and finally to 70 to 80% for 1Fe clusters.

4.5. Redox Potentials for Clusters in Solvent. Table 8 summarizes our redox potential calculations, based on eq 1. For all of these systems, the gas phase ionization potential of the reduced complex (IP(red)) is negative, reflecting the difficulty (in vacuum) of adding an extra electron to a transition metal complex that is already negatively charged. By contrast, the large positive solvation energy contributions reflect the much stronger solvation of the more reduced species in each case.

A global comparison of our calculations (using $\epsilon = 37$) with experiment[10,70,71] is given in Table 9 and Figure 4. Overall the

---

(67) Aizman, A.; Case, D. A. *J. Am. Chem. Soc.* **1982**, *104*, 3269−3279.

(68) Case, D. A. *Annu. Rev. Phys. Chem.* **1982**, *33*, 151−171.

(69) Case, D. A.; Cook, M.; Karplus, M. *J. Chem. Phys.* **1980**, *73*, 3294−3313.

(70) DePamphilis, B. V.; Averill, B. A.; Herskovitz, T.; Que, L.; Holm, R. H. *J. Am. Chem. Soc.* **1974**, *96*, 4159−4167.

Table 7. Comparison of Solvation Energies from Mulliken and ESP Charges

		Mulliken[a]		ESP[a]	
system	state	RMS (rd/ox)	ΔE_{PB}(solv)	RMS (rd/ox)	ΔE_{PB}(solv)
$[Fe(SCH_3)_4]^{2-,1-}$		0.0073/0.0065	+5.50	0.0048/0.0042	+5.52
$[Fe_2S^*_2(SCH_3)_4]^{3-,2-}$		0.0104/0.0093	+8.50	0.0053/0.0050	+8.38
$[Fe_4S^*_4(SCH_3)_4]^{3-,2-}$	OC2 (relaxed)	0.0095/0.0087	+7.63	0.0058/0.0054	+7.57
$[Fe_4S^*_4(SCH_3)_4]^{2-,1-}$	OS3 (D_{2d})	0.0087/0.0080	+4.71	0.0054/0.0050	+4.67

[a] Units: RMS (rd/ox) in au/e^- (1 au/e^- = 27.21 V), and ΔE_{PB}(solv) in eV.

Table 8. Calculated Redox Potentials

system	state	ϵ	IP (red)	ΔE_{PB} (solv)	E°
$[Fe(SCH_3)_4]^{2-,1-}$		37	−1.79	+5.52	−0.77
		80	−1.79	+5.59	−0.70
$[Fe_2S^*_2(SCH_3)_4]^{3-,2-}$		37	−5.27	+8.38	−1.38
		80	−5.27	+8.51	−1.26
$[Fe_4S^*_4(SCH_3)_4]^{3-,2-}$	OC1 (D_{2d})	37	−4.91	+7.62	−1.79
		80	−4.91	+7.73	−1.68
	OC1 (relaxed)	37	−4.71	+7.54	−1.67
		80	−4.71	+7.66	−1.56
	OC2 (D_{2d})	37	−4.82	+7.63	−1.69
		80	−4.82	+7.75	−1.58
	OC2 (relaxed)	37	−4.63	+7.57	−1.56
		80	−4.63	+7.69	−1.45
$[Fe_4S^*_4(SCH_3)_4]^{2-,1-}$	OS1 (D_{2d})	09	−0.50	+4.25	−0.75
		37	−0.50	+4.67	−0.33
		80	−0.50	+4.74	−0.26
	OS1 (C_{2v})	09	−0.18	+4.24	−0.44
		37	−0.18	+4.66	−0.02
		80	−0.18	+4.73	+0.05
	OS2 (D_{2d})	09	−0.23	+4.27	−0.47
		37	−0.23	+4.69	−0.04
		80	−0.23	+4.76	+0.03
	OS2 (C_{2v})	09	+0.16	+4.24	−0.10
		37	+0.16	+4.66	+0.32
		80	+0.16	+4.73	+0.38
	OS3 (D_{2d})	09	−0.17	+4.25	−0.43
		37	−0.17	+4.67	0.00
		80	−0.17	+4.74	+0.07
	OS3 (C_{2v})	09	+0.42	+4.23	+0.15
		37	+0.42	+4.64	+0.56
		80	+0.42	+4.71	+0.63

correlation between theory and experiment is good, and these are "absolute" redox calculations. Experimentally, the redox potentials of these synthetic clusters span a total range of about 1.6 eV from about −1.24 to +0.34 eV. The reduced 2Fe,3−/2− and 4Fe,3−/2− redox couples have the most negative redox potentials, covering overlapping ranges, followed by the 1Fe,2−/1−, and finally with the oxidized HP couple 4Fe,2−/1− at the most positive potential. The theoretical calculations (with $\epsilon = 37$ as in DMF) give a similar total span of about 1.67 eV, with similar ordering, ranging from the reduced 4Fe,3−/2− to 2Fe,3−/2− at somewhat higher potential, followed by 1Fe,2−/1−, and finally by the electronic states for the oxidized HP couple 4Fe,2−/1−. The maximum calculation error is about −0.5 eV compared to experiment, with a range of error from 0.0 to −0.5 eV, or generally less than 10% of the related solvation energy difference ΔE_{PB}. The total span of redox potentials in related proteins is smaller, about 0.85 eV, and positively shifted by about +0.5 eV with respect to synthetic clusters, but the relative redox potential ordering of different clusters and oxidation states is very similar to that of the synthetic clusters.[72] We can conclude that the calculated absolute redox potentials for these clusters in solvent are in reasonably good agreement with experiment for analogous synthetic clusters, particularly given the difficulties in accurately calculating a sum of large terms in general having different signs (Tables 8−10, Figure 5). These terms are often 1 order of magnitude or more larger than the final calculated redox potential.

4.6. Relation to Born Solvation Model. In the Born model for solvation, the solvation energy difference of the oxidized minus reduced state is given by $-[(Q_{ox}^2 - Q_{red}^2)/2R_{eff}](1 - (1/\epsilon))$, where the Q's are the total molecular charges, and R_{eff} is the effective molecular radius of the molecule. (R_{eff} can be approximated as a spherical cavity encompassing the van der Waals envelope around the atoms.) The ratio of solvation energies for the 2−,3− couple versus the 2−,1− couple for 4Fe4S systems should then be approximately $^5/_3$, since the molecular radius does not vary much among the three oxidation states. The calculated ratio obtained directly from solution of the Poisson−Boltzmann equation for our complicated molecular shape gives a ratio of ΔE_{PB}(solv) as 1.63 at both $\epsilon = 37$ and $\epsilon = 80$. (The D_{2d} geometry of the 4Fe, 2− complex was used throughout; the ratio is insensitive to the specific orbital configurations used for the 1− and 3− redox states.) This is entirely consistent with the simple Born model for these systems.

Another aspect of the Born equation above is the simple dependence of the solvation energy difference on the dielectric constant ϵ, which can be checked both against the more complex Poisson-Boltzmann result, and against the experimentally observed dependence of cluster redox potentials on solvent. For the 4Fe,2−/1− couple, the ratios from the Born equation for the solvation energy difference at $\epsilon = 9$, 80 to that at $\epsilon = 37$ are 0.91, 1.02, respectively. The Born equation prediction for ΔE_{PB} with $\epsilon = 9$, 80 starting from the calculated ΔE_{PB} for $\epsilon = 37$ almost exactly corresponds to the values directly calculated. For example, the Born equation for OS1 (D_{2d}) predicts solvation energy differences of +4.27, +4.74 eV for $\epsilon = 9$, 80 starting from +4.67 eV ($\epsilon = 37$) compared to +4.25, +4.74 by direct calculation (ΔE_{PB}, Table 8). Similar agreement is found in the predicted shift of OC2(D_{2d}) ΔE_{PB} from +7.63 eV ($\epsilon = 37$) to +7.75 eV ($\epsilon = 80$) by the Born formula or actual calculation.

While the Poisson−Boltzmann energies behave precisely as expected theoretically as a function of ϵ, the experimental behavior is more complicated. The predicted positive shift in redox potential with increasing ϵ of the solvent is not found experimentally with any uniformity. In fact, work by Blonk and co-workers[73] and earlier work summarized by Zanello[74] shows that experimental redox shifts of 4Fe4S clusters in solvent are not at all monotonic with dielectric constant and can differ by 0.2 eV for solvents with nearly equal dielectric constants like acetonitrile and *N*,*N*-dimethylformamide, both with $\epsilon = 37$. Further, the positive shift observed in going from methanol ($\epsilon = 32.6$), DMF, or DMSO ($\epsilon = 47.1$) to water ($\epsilon = 78.5$) can be as large as 0.5 eV, far more positive than the 0.1 eV shift predicted theoretically. It is therefore, likely that the detailed molecular structure of the solvent is important for the finer scale aspects of redox potentials. Whether this is a result of bonding

---

(71) Mascharak, P. K.; Hagen, K. S.; Spence, J. T.; Holm, R. H. *Inorg. Chim. Acta* **1983**, *80*, 157−170.

(72) Xavier, A.; Moura, J. J. G.; Moura, I. *Struct. Bonding* **1981**, *43*, 187−213.

(73) Blonk, H. L.; Kievit, O.; Roth, E. K. H.; Jordanov, J.; van der Linden, J. G. M.; Steggerda, J. J. *Inorg. Chem.* **1991**, *30*, 3231−3234.

(74) Zanello, P. *Coord. Chem. Rev.* **1988**, *83*, 199−275.

Table 9. Comparison of Calculated and Experimental Redox Potentials[a,b]

cluster	technique		redox potential (eV)
$[Fe(SR)_4]^{2-,1-}$	density functional	$\epsilon = 37$	−0.77
		$\epsilon = 80$	−0.70
	synthetic cluster (expt)	R = *o*-xylyl	−0.79
	protein (expt)	rubredoxin (1Fe)	−0.06
$[Fe_2S^*_2(SR)_4]^{3-,2-}$	density functional	$\epsilon = 37$	−1.38
		$\epsilon = 80$	−1.26
	synthetic cluster (expt)	R = *o*-xylyl	−1.25
		R = phenyl	−0.85
	protein (expt)	ferredoxin (2Fe)	−0.24 to −0.43
$[Fe_4S^*_4(SR)_4]^{3-,2-}$	DF:OC1 (rel)	$\epsilon = 37$	−1.67
		$\epsilon = 80$	−1.56
	DF:OC2 (rel)	$\epsilon = 37$	−1.56
		$\epsilon = 80$	−1.45
	synthetic cluster (expt)	R = methyl	−1.05
		R = *tert*-butyl	−1.18
	peptides	nonapeptide	−0.58
	and proteins (expt)	dodecapeptide	−0.56
		ferredoxin (4Fe)	−0.28 to −0.42
		ferredoxin (8Fe)	−0.40 to −0.49
		HIPIP	≤ −0.64
$[Fe_4S^*_4(SR)_4]^{2-,1-}$	DF:OS1 (D_{2d})	$\epsilon = 09$	−0.75
		$\epsilon = 37$	−0.33
		$\epsilon = 80$	−0.26
	DF:OS2 (D_{2d})	$\epsilon = 09$	−0.47
		$\epsilon = 37$	−0.04
		$\epsilon = 80$	+0.03
	DF:OS3 (D_{2d})	$\epsilon = 09$	−0.43
		$\epsilon = 37$	0.00
		$\epsilon = 80$	+0.07
	synthetic cluster (expt)	R = *tert*-butyl	peak 1: +0.10 peak 2: +0.34
	protein (expt)	HIPIP	+0.34

[a] All synthetic cluster values were converted to SHE reference values by adding +0.24 V to standard calomel electrode (SCE) measurements. [b] All redox values taken from Holm and Ibers, 1977,[10] except 4Fe,3−/2− (R = methyl) from DePamphilis et al., 1974,[70] and 4Fe,2−/1− from Mascharak et al., 1983.[71]

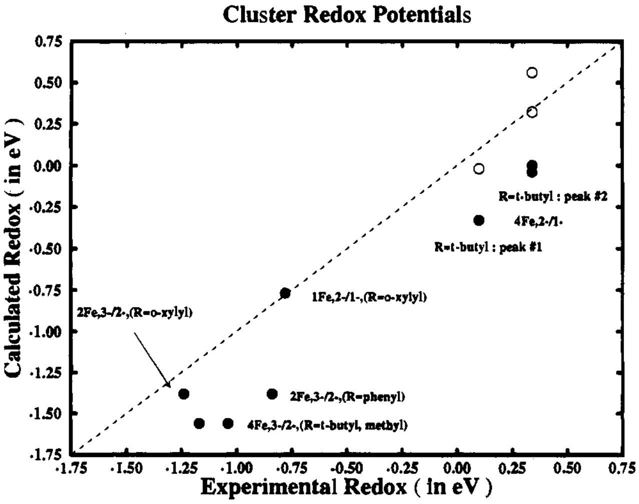

Figure 4. Calculated vs experimental cluster redox potentials. The dotted line is the line of identity between calculated and experimental values. For 4Fe,1−: solid circles, D_{2d} geometry; open circles, C_{2v} geometry.

between the cluster and solvent, specific hydrogen-bonding interactions, electron donation, solvent size, or boundary layer effects, among other possibilities, is unknown, but there are clear indications of limitations to the continuum dielectric method.

4.7. Comparative Contributions of Solvation, Spin Coupling, and Electron Delocalization to Redox Potentials. The correlation found between calculated and experimental redox potentials provides a sound foundation for asking the next question: what terms contribute to the redox potential, and what are their relative sizes and effects? Figure 5 and Table 10 deal with this question. While the earlier analysis separated simply the IP(red) and ΔE_{PB} terms (Table 8), we can also use the spin barycenter concept to partition the spin coupling (ΔJT) and electron delocalization (ΔBT) terms, as shown in Table 10. Figure 5a shows the redox potential calculated with four successive sets of terms (I through IV) compared with experiment (V). Figure 5b,c shows II−V on an expanded scale, treating the oxidized high potential cluster in symmetry D_{2d} (Figure 5a,b), and C_{2v} (Figure 5c) geometries. In Figure 5a, the first column (I) gives E_{un}(vac), the redox potentials for the clusters in vacuum with interlayer spin coupling and intralayer electron delocalization effects removed. E_{un}(vac) redox potentials are very negative, because solvation is absent, and span a large range (over 4 eV) from −5.3 to −9.4 eV. They are ordered as one would expect from internal charge−charge repulsion based on cluster sizes and total charges.

The addition of solvation produces an enormous positive shift in the potentials of all clusters. In II, the sum $E^{\circ}_{un} = E_{un}(vac) + \Delta E_{PB}$ is evaluated, which shows the large compensating effects of solvation, counteracting internal repulsion; this compensation is nearly complete in the sense that the span of redox energies is greatly reduced to 0.6 eV (range −0.98 to −0.40 eV). Addition of ΔBT in III has no effect on the 1Fe and 2Fe systems (Figure 5b,c), since these are trapped valence in the reduced state. However, there are significant positive shifts for all 4Fe,2−/1− states and negative shifts of comparable magnitude for all 4Fe,3−/2− states, about ±0.5 eV. This occurs because of the presence of two resonance delocalized pairs in alternate Fe−Fe layers for the 4Fe,2− state while 4Fe,1− and 4Fe,3− have only one delocalized pair in each system. Thus, the reduced state of the 4Fe,2−/1− couple is stabilized by delocalization, producing a positive shift, but this same state is

Table 10. Analysis of Calculated Redox Potentials[a]

system	state	ϵ	E_{un}(vac)	ΔE_{PB}	E^0_{un}	ΔBT	ΔJT	$E°$
$[Fe(SCH_3)_4]^{2-,1-}$		37	−6.29	+5.52	−0.77	no	no	−0.77
		80	−6.29	+5.59	−0.70	no	no	−0.70
$[Fe_2S^*_2(SCH_3)_4]^{3-,2-}$		37	−9.36	+8.38	−0.98	no	−0.41	−1.38
		80	−9.36	+8.51	−0.85	no	−0.41	−1.26
$[Fe_4S^*_4(SCH_3)_4]^{3-,2-}$	OC1 (relaxed)	37	−7.94	+7.54	−0.40	−0.56	−0.73	−1.67
		80	−7.94	+7.66	−0.28	−0.56	−0.73	−1.56
	OC2 (relaxed)	37	−8.03	+7.57	−0.46	−0.52	−0.58	−1.56
		80	−8.03	+7.69	−0.34	−0.52	−0.58	−1.45
$[Fe_4S^*_4(SCH_3)_4]^{2-,1-}$	OS1 (D_{2d})	37	−5.59	+4.67	−0.92	+0.47	+0.11	−0.33
		80	−5.59	+4.74	−0.85	+0.47	+0.11	−0.26
	OS2 (D_{2d})	37	−5.47	+4.69	−0.78	+0.48	+0.26	−0.04
		80	−5.47	+4.76	−0.71	+0.48	+0.26	+0.03
	OS3 (D_{2d})	37	−5.30	+4.67	−0.63	+0.50	+0.13	+0.00
		80	−5.30	+4.74	−0.56	+0.50	+0.13	+0.07

[a] Values in eV.

the oxidized state of the 4Fe,2−/3− couple, so that resonance delocalization leads to a negative shift.

The final calculated redox potential is obtained in IV, where the ΔJT contribution has been added to the previous sum. For 4Fe systems, the ΔJT term produces small positive shifts for 4Fe,2−/1− and larger negative shifts for 4Fe,3−/2−. From the spin barycenter equations (Table 4), the shift for 4Fe,2−/1− is given by $25J_{\mathrm{m}} - 22J_{\mathrm{ox}}$, and that for 4Fe,3−/2− by $22J_{\mathrm{red}} - 25J_{\mathrm{m}}$. If all J values were equal, this would produce equal shifts of opposite sign, but since $J_{\mathrm{ox}} \geq J_{\mathrm{m}} > J_{\mathrm{red}}$, the negative shifts are larger. Overall, the combination of the ΔBT and ΔJT terms has an important influence in separating the redox potentials of the reduced 4Fe,3−/2− and high potential 4Fe,1−/2− couples, making the high potential couple more positive than the reduced couple.

4.8. Redox Potentials for 1Fe and 2Fe Complexes. For 2Fe,3−/2−, the ΔJT shift to the redox potential is also negative from the difference $-9J_{\mathrm{ox}} + 7J_{\mathrm{red}}$, noting also $J_{\mathrm{ox}} > J_{\mathrm{red}}$. Bertrand and Gayda[75] originally proposed the presence of a negative shift to the redox potential of 2Fe,3−/2− complexes compared with 1Fe,2−/1− due to antiferromagnetic coupling. Our results provide support for their original idea, along with some modifications of the equations involved (see below), and calculated values. Using our calculated J values, $J_{\mathrm{ox}} = 763$ cm^{-1}, $J_{\mathrm{red}} = 514$ cm^{-1}, we calculate a redox shift of $\Delta JT = -0.41$ eV. In 2Fe,3−/2− systems, experimental J values are available from magnetic susceptibility measurements in proteins;[76] more indirectly, J values have been obtained from spin−lattice relaxation measurements in proteins, and in synthetic analogues.[77] As an example, we will calculate the shift in redox potential due to the ΔJT term using the experimental J values from *Spirulina maxima* 2Fe2S protein, $J_{\mathrm{ox}} = 364$ cm^{-1}, $J_{\mathrm{red}} = 196$ cm^{-1}.[76] The calculated shift is $\Delta JT = -0.24$ eV; this semiempirical shift is less than the theoretical calculated shift of −0.41 eV, because the corresponding experimental J values are smaller than those we have calculated from density functional methods. Bertrand has computed a semiempirical shift of −0.43 eV,[75] about twice the size of ours. With the same average experimental J values he used from plant ferredoxins, ($J_{\mathrm{ox}} = 360$, $J_{\mathrm{red}} = 160$) we would obtain −0.26 eV. The reason for this descrepancy is that Bertrand has calculated the ΔJT stabilization using the high spin state as the "uncoupled" reference state, rather than using the spin barycenter state. In the high-spin state, all the magnetic orbitals on one iron site must be orthogonal to all the magnetic orbitals on the other site because the spin vectors for the two sites are parallel. This is an antibonding situation which we refer to as "spin−antibonding". By contrast, the spin barycenter energy represents a weighted average of spin vector alignments and is effectively "spin−nonbonding". The spin barycenter therefore provides a better "nonbonded" reference state. From Table 10, the ΔJT term provides about $^2/_3$ of the calculated shift (−0.6 eV) in redox potential on going from 1Fe,2−/1− to 2Fe,3−/2− couples. Using the semiempirical shift of $\Delta JT = -0.24$ to −0.26 eV gives a difference of about −0.4 eV between 2Fe,3−/2− and 1Fe,2−/1− couples, which is in good agreement with the differences experimentally observed between rubredoxins and 2Fe ferredoxins.

Finally, we should note that in the single 2Fe2S synthetic system where experimental J_{ox}, J_{red} values have been measured, and where comparable redox potential measurements have been made for both 1Fe and 2Fe complexes, $Fe(S_2\text{-}o\text{-}xyl)_2^{1-,2-}$ and $Fe_2S_2(S_2\text{-}o\text{-}xyl)_2^{2-,3-}$ the value of J_{red} is anomalous. The observed redox potential shift from the 1Fe,2−/1− to the 2Fe,3−/2− complex is −0.46 eV, about as expected. However, the measured $J_{\mathrm{red}} = 600$ cm^{-1} [77] is much greater than $J_{\mathrm{ox}} = 298$ cm^{-1}.[76] This trend is anomalous compared to the observation ($J_{\mathrm{ox}} > J_{\mathrm{red}}$) in all proteins studied, and the associated negative redox potential shift from 1Fe to 2Fe proteins. However, the J_{ox} measurements were made by magnetic susceptibility, while J_{red} was obtained by fitting observed EPR spin lattice relaxation times to find the excited $S = {}^3/_2$ state (assuming a dominant Orbach mechanism). It is not clear that the excited spin state position must be the same by the two methods. For example, magnetic susceptibility reflects the position of excited states found by a thermal process (adiabatic excited state), while Orbach relaxation involves a virtual excited spin state. Further comparisons of J_{red} parameters obtained by both magnetic susceptibility and spin lattice relaxation measurements in the same systems in conjunction with redox potential measurements would be very valuable in improving our understanding of these interrelated phenomena.

4.9. Redox Properties of High Potential 4Fe4S Clusters. From Tables 8−10 and Figures 4 and 5, it is clear that the three different states OS1, OS2, and OS3 have different predicted redox potentials. With D_{2d} geometry, the predicted redox potentials range from −0.33 eV (OS1) to −0.04 eV (OS2) to 0.0 eV (OS3) for $\epsilon = 37$. This suggests that one should look for the presence of closely spaced electronic states in redox potential measurements of related synthetic analogues. Mascharak and co-workers have measured redox potentials of various 4Fe,2−/1− complexes with R = *tert*-alkyl substituents.[71] In differential pulse polarograms of the R = *tert*-butyl synthetic complex, two well-defined peaks equivalent to +0.10, +0.34 V vs SHE were observed before massive oxidation and cluster

---

[75] Bertrand, P.; Gayda, J. P. *Biochim. Biophys Acta* **1982**, *680*, 331−335.

[76] Petersson, L.; Cammack, R.; Rao, K. K. *Biochim. Biophys. Acta* **1980**, *622*, 18−24.

[77] Beardwood, P.; Gibson, J. F. *J. Chem. Soc. Dalton* **1983**, 737−748.

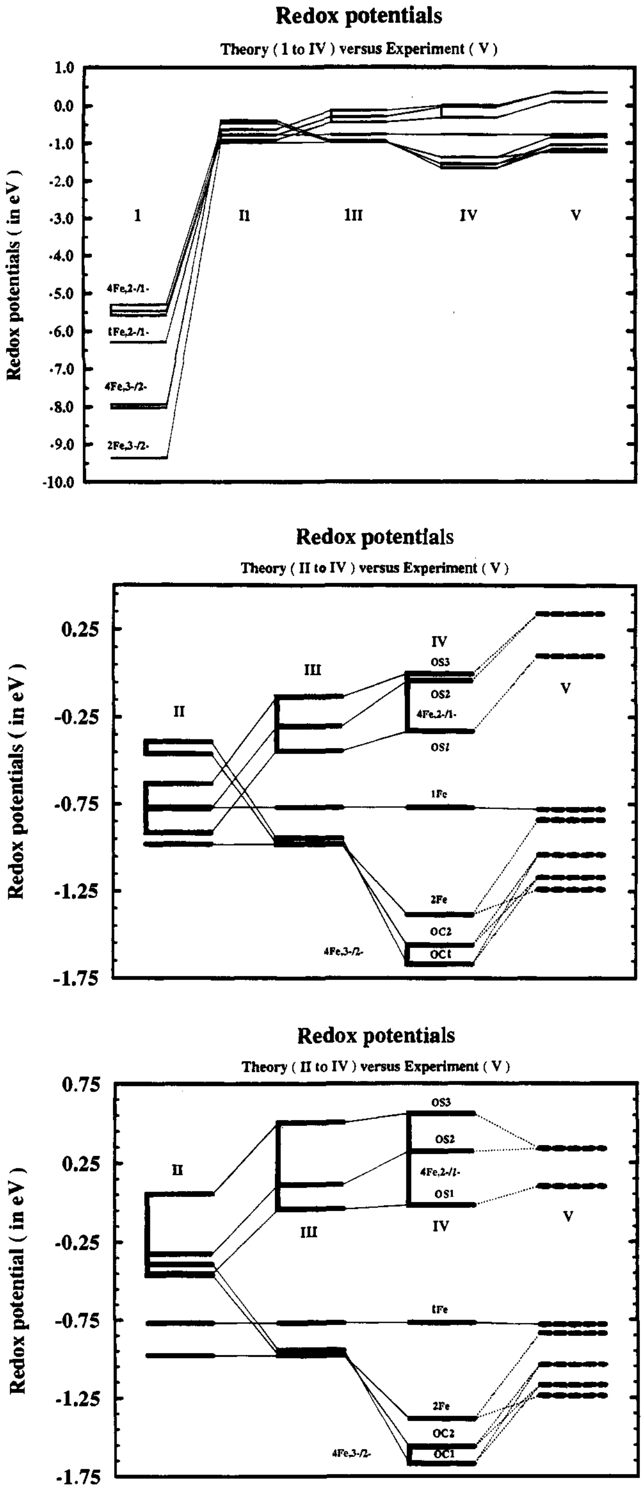

Figure 5. Contributions to redox potentials for 1Fe, 2Fe, and 4Fe clusters. Contributions: I = $E_{\mathrm{un}}(\mathrm{vac})$; II = $\overset{\circ}{E}_{\mathrm{un}} = [E_{\mathrm{un}}(\mathrm{vac}) + \Delta E_{\mathrm{PB}}]$; III = $[\overset{\circ}{E}_{\mathrm{un}} + \Delta BT]$; IV = $[\overset{\circ}{E}_{\mathrm{un}} + \Delta BT + \Delta JT] = E^\circ$; V = experimental values. The parts of the figure are as follows: (a) Theoretical contributions I–IV vs experiment V. (b,c) contributions II–IV vs experiment V on expanded scale. (For HP_{ox}, a and b are for D_{2d} geometry, and c is for C_{2v} geometry.)

decomposition at higher oxidizing potential. These peaks may be associated with two (or all three) of the electronic states OS1, OS2, or OS3 as assigned in Figures 4 and 5. The isolation and spectroscopic characterization of the different species observed by differential pulse polarography using EPR, Mossbauer, or ENDOR techniques would be very interesting. The presence of these two peaks in the polarogram is dependent on the R group and is not seen with other substituents. It does appear likely that the ordering and spacing of the close lying electronic states OS1, OS2, and OS3 will depend strongly on the R group, or environment. Further, quantum mixing of these states by spin–orbit coupling is also possible.

It is certainly unusual to observe different electronic states at the same oxidation state level by electrochemical measurements, so we consider these possibilities in more detail. In principle, the two well-defined peaks observed for R = *tert*-butyl could arise either (1) from two successive one-electron oxidations of the 4Fe,2− species or (2) from alternative one-electron oxidations yielding two different electronic final states (possibly with geometric differences as well). The first alternative seems unlikely, both because the two peaks are closely spaced with only +0.24 V between them, and, more importantly, because a stable (or metastable) $[Fe_4S_4(SR)_4]^0$ species is unknown for any ligand type (all four iron sites formally Fe^{3+}). For the second alternative, the different redox potentials must arise from electronic heterogeneity in the final oxidized state (1−). Heterogeneity in the reduced (2−) state is excluded because one-electron reduction to the (3−) form gives one peak only.[71] Kinetically, the rate of electron removal, upon oxidation to the higher energy final state (more positive redox potential) must occur more rapidly than electronic relaxation (either by radiative or nonradiative decay) to the lower energy state (less positive redox potential). This is consistent with the spin-forbidden character of the OS1, OS2 → OS3 transition (or conversely, OS3 → OS1, OS2), which would indicate a slow interconversion. By contrast, OS1 ↔ OS2 is spin allowed, so interconversion should be rapid, and only one peak would be expected from these two electronic states.

Despite the plausibility of the argument above, this is clearly a problem where further experimental studies could be decisive in understanding the underlying phenomena. Specifically, cyclic voltammetry can quantitate the number of electrons removed that are associated with each peak, and would then decide between the alternative versus successive oxidation hypotheses. Different scan rates and cycling over more oxidizing and then more reducing potentials should confirm which peaks are thermodynamically stable (these would appear on oxidation and on reduction) compared to those which are only kinetically stable or metastable (these would appear only on oxidation, and/or would be strongly sensitive to the scan rate).

4.10. Redox Properties of Reduced 4Fe4S Clusters. The states OC1 and OC2 are calculated to be very close in energy. Corresponding to this, the redox potentials predicted for these two states are quite close (Table 10), separated only by 0.1 eV with the OC2 state slightly lower in energy (at more positive potential). The solvation energies of these two states are quite similar, despite their differences in orbital structure. As shown in Table 2, the ratio $B'/J_{\mathrm{red}} \geq 3/2$ controls the $S = 1/2$ vs $S = 3/2$ equilibrium for the fully delocalized state, with the larger ratios giving an $S = 3/2$ ground state, while $-\Delta E(S)_{\mathrm{solv(pf)}} \geq (S + 1/2)|B'|$, determines the energy balance between pairwise vs fully delocalized forms for a specified spin state S. (Here $\Delta E(S)_{\mathrm{solv(pf)}}$ is the solvation energy difference for the two forms, and is negative when the pairwise form is better solvated, as expected.) Some numbers will make these ideas more concrete (Table 3). The calculated $B'/J_{\mathrm{red}} = 1.2$ for OC2, but 0 for OC1, compared with the crossover point at 1.5. The OC2 value is near the spin crossover point from $S = 1/2$ to $S = 3/2$ for full delocalization, and this ratio will be larger if the theoretical J_{red} is overestimated, as is typical at least for 2Fe2S systems. The magnitude of B' = 0.077 eV implies that the pairwise delocalized to fully delocalized equilibrium is very sensitive, and requires accurate evaluation of $-\Delta E(S)_{\mathrm{solv(pf)}}$. This is beyond our current numerical accuracy for ΔE_{PB}. By quenching the B' term, the pairwise delocalized situation favors $S = {}^{1}/_{2}$ over $S = {}^{3}/_{2}$. While further quantitative work is needed, at a more qualitative level, these ideas may be relevant to the spin equilibria of $S = {}^{1}/_{2}$ and ${}^{3}/_{2}$ observed in *Pyrococcus furiosus* ferredoxin protein where there is conformational heterogeneity, and where the $S = {}^{1}/_{2}$ structural form displays greater solvent accessibility than the $S = {}^{3}/_{2}$ form.[2] Finally, we note that the energy stabilization within a delocalized mixed valence pair $5B$ exceeds B' or $2B'$ for all the clusters studied. Thus resonance delocalization within a pair (intralayer) is far more robust against localization than is the B' resonance (interlayer), in agreement with Mossbauer spectroscopic results that indicate that pairwise equivalence, particularly within the mixed valence pair, is more common than complete equivalence among all iron sites.[55,56,78]

5. Conclusions

Figures 4 and 5 and Tables 8−10 provide summaries of our major results for redox potentials. Tables 5 and 6 summarize our final charge models using the electrostatic potential (ESP) fitting algorithm. Our main conclusions are as follows:

(1) There is a good correspondence between calculated and experimental redox potentials of synthetic 1Fe, 2Fe, and 4Fe clusters both with respect to relative ordering and with respect to relative redox energies (total energy span and spacing). The largest error comparing calculated (R = methyl) and experimental systems is about 0.5 eV (calculated more negative). Overall, there is a systematic error of about 0 to −0.5 eV; this error is less than 10% of some of the contributing terms, particularly the solvation energy difference term (ΔE_{PB}) which can range from 4.5 to 8.5 eV.

In response to a reviewer's comments, we note that the solvation energy difference is a free energy difference at finite temperature. (T is near 25 K for typical tabulated dielectric constants for water and organic solvents.) We have not included the free energy contribution from the entropy term $RT \ln(Q)$ of thermally occupied excited spin states, or the electronic degeneracy factor of the spin ground state (spin multiplicity, $Q_{ox,red} = (2S + 1)$ for the oxidized, reduced states) but these effects are comparatively small. For example, in a redox transition from an $S = 0$ to an $S = {}^{3}/_{2}$ state, the $RT \ln(Q_{red}/Q_{ox})$ contribution to the redox potential is 0.036 eV; this is quite small compared with the size of energy terms we are evaluating, and the present accuracy of our methods. Thermally populated excited spin states would be expected to make a comparatively small contribution as well, for typical J values in FeS systems. Probably, the effects of changes in zero-point vibrational energies, and of geometric relaxation upon redox change in solvent are more important than electronic configurational entropy effects, and should be considered in future work.

(2) Using the spin and electron delocalization barycenter concept, we have partitioned the final calculated redox potential into a sum of terms. The most important consequences of this analysis are (a) the solvation energy difference terms are very large, but their overall effect is to compensate almost completely for the differences in charge−charge repulsion among different cluster forms and redox couples; (b) the Heisenberg spin coupling contribution (ΔJT) to the redox potential produces a negative potential shift in 2Fe complexes. While smaller than the solvation term, it makes a major contribution to the more negative redox potentials observed in 2Fe complexes and proteins compared with related 1Fe systems; (c) in 4Fe4S systems, the presence of one resonance delocalized pair in both oxidized high potential and reduced clusters, compared with two resonance pairs in the 4Fe,2− state, leads to a substantial positive shift (ΔBT about +0.5 eV) of the HP couple, and a comparable negative shift (−0.5 eV) of the reduced couple. The ΔJT term acts in the same direction as ΔBT in each case with smaller magnitude (about +0.15 eV) for the HP and larger effect (about −0.6 eV) for the reduced couple. The net effect is that the large difference in redox potentials between the 4Fe,2−/1− $HP_{ox,red}$ and the 3−/2− $Fd_{ox,red}$ couple has a very substantial contribution from the combined $\Delta JT + \Delta BT$ terms.

We note that the variation in redox potentials of synthetic 4Fe4S clusters with solvent type is not a unique or monotonic function of the solvent dielectric constant,[73] so that some cluster−solvent interactions must occur where the solvent molecular structure is relevant. The size of the solvation energy difference term ΔE_{PB} is so large that small percentage differences in these can give considerable fine-tuning to redox potentials. Analogously, in proteins, protein electrostatic, solvent, and dielectric influences exert considerable effects on redox potentials. Nonetheless, spin coupling and electron delocalization terms exert a large and systematic effect in both 2Fe2S and 4Fe4S complexes, and these effects are paralleled by trends in observed redox potentials both in synthetic complexes and in proteins.

The large size of hydrogen bonding, electrostatic, and solvation energy terms has consequences in proteins. The observations from X-ray crystallography of structural differences including a greater number of hydrogen bonds and greater solvent exposure for the 4Fe cluster in ferredoxin proteins compared to HP proteins probably contributes to the greater energetic stability of the 3− oxidation state in ferredoxin proteins than in HP proteins, when considering the same 2−/3− redox couple, as postulated by Carter, Adman, and coworkers.[14,79,80]

(3) For the synthetic analogue to HP_{ox}, calculated with R = methyl, we have found three low lying states (OS1, OS2, and OS3) within about 0.3 eV of each other. Any of these are potentially the ground electronic state in synthetic systems or in proteins. OS3, which contains a high spin ferric pair antiferromagnetically coupled to a high spin mixed valence pair (with additional spin canting within $2Fe^{3+}$), has been assumed to be the ground state in our previous spin Hamiltonian work. Further, the calculated **g** tensor for OS3 is rather like those observed in experimental protein and synthetic systems,[12,55,66,81] although there is a fair degree of variability depending on detailed conditions. However, OS1 and OS2 have lower calculated energies for R = methyl; these contain an intermediate spin $2Fe^{3+}$ pair, where each site is alternately intermediate or high spin $S_1, S_2 = {}^{3}/_{2}, {}^{5}/_{2}$. These states are related to OS3 by single spin forbidden Fe d → d and S,S* → Fe charge transfer transitions. There is also experimental evidence for two distinct and well-resolved redox potentials separated by only 0.24 eV for the synthetic HP_{ox} system with R = *tert*-butyl. We interpret these in terms of the three closely spaced electronic states that we have found. These results could have significant implications in understanding the electronic structure and spin coupling of the HP_{ox} cluster form in both proteins and synthetic analogues.

(4) The ESP charges demonstrate that the Fe atoms become effectively more positive as the clusters are reduced, and that all S,S* atoms become considerably more negative. Since the active orbital involved in most cases (with the exceptions of

---

[78] Middleton, P.; Dickson, D. P. E.; Johnson, C. E.; Rush, J. D. *Eur. J. Biochim.* **1978**, *88*, 135−141.

[79] Backes, G.; Mino, Y.; Loehr, T. M.; Meyer, T. E.; Cusanovich, M. A.; Sweeny, W. V.; Adman, E. T.; Sanders-Loehr, J. *J. Am. Chem. Soc.* **1991**, *113*, 2055−2064.

[80] Sheridan, R. P.; Allen, L. C.; Carter, C. W. *J. Biol. Chem.* **1981**, *256*, 5052−5057.

[81] Rius, G.; Lamotte, B. *J. Am. Chem. Soc.* **1989**, *111*, 2464−2469.

4Fe,1−, OS1, and OS2 → 4Fe,2−) are mainly centered on iron, electron relaxation effects upon reduction are large, arising from collective changes in the passive orbitals. These strong electron relaxation effects are the main cause of the compensation found between solvation energy differences and charge−charge repulsion. As a consequence, most of the electron density increase on reduction occurs at S,S* which lie toward the outside in all clusters, and are exposed to solvent, which screens the increased electron−electron repulsion effectively. Higher Fe−S bond polarities are found from the ESP charges than from Mulliken charges, but the changes in charges upon oxidation or reduction are similar in magnitude and sign with either method. Despite the higher bond polarity of the ESP charges, Mulliken charges give quite similar solvation energy differences ΔE_{PB} to ESP (Table 7). Nonetheless, on the basis of the better RMS of the fit, the ESP charges should be the most reliable and transferable charge sets for other electrostatic calculations in FeS proteins.

There is now some experience in using charge models from density functional calculations to calculate comparative redox shifts of related 2Fe2S and 4Fe4S proteins. Langen and coworkers[82] have calculated redox shifts successfully among related 4Fe,3−/2− proteins using a "protein dipoles Langevin dipoles" model, and charges from our earlier Xα scattered wave calculations on 4Fe4S clusters.[42] Smith and co-workers[83] have analyzed the redox shift in *Clostridium pasteurianum* ferredoxin when a histidine (obtained with site substitution, tyrosine-2 → histidine-2) near the 4Fe4S cluster is protonated. Ludwig and co-workers[84] have compared the contribution of electrostatic interaction energies from different residues to the redox potential shift of phthalate dioxygenase reductase (PDR) with respect to that in *Anabaena* ferredoxin. The 2Fe2S charge models in Ludwig's work were obtained directly from the ESP charges given in the present work (see Table 5). The transferability of charge parameters from density functional calculations on clusters to protein electrostatic redox potential calculations is quite promising. In addition to work in this direction, we have also recently developed both methodology and computer programs which allow the electronic structure of the active site cluster to change in response to the solvent reaction field, and to iteratively solve this problem, creating a self-consistent reaction field (SCRF).[85] Further work both on clusters in solvent and in protein environments is planned.

Acknowledgment. We gratefully acknowledge helpful discussions with P. Bertrand, J. Jordanov, E. Roth, B. Lamotte, K. Hagen, M. Ludwig, and G. Jensen. This work was supported by NIH grant GM39914, and by a NATO travel grant to D.A.C., L.N., and B. Lamotte. J.M.M. gratefully acknowledges additional support from the French Ministry of Foreign Affairs through a Lavoisier grant (from 12/91 to 12/92). We thank E. J. Baerends for use of the ADF density functional programs, and P. Vernooijs and G. te Velde for technical assistance.

Appendix. Singular Value Decomposition Analysis of Charges.

In the standard determination of least-squares fit charges using the CHELPG algorithm, the required matrix inversion is performed by a Gauss−Jordan elimination procedure, but this gives little indication of how close the matrix to be inverted is to being singular. One would like to have some understanding of how unique and well-defined the point charge fit is, and what the expected uncertainties of the calculated solvation energies are. Singular value decomposition provides a tool to study these issues.[35]

Specifically, the total Coulomb potential generated by a set of point charges (q_j) can be fit to the electrostatic potential (V_i^{MEP}) obtained from the quantum mechanical charge density. LaGrange multipliers (λ_j) are introduced for the charge and dipole moment constraints. The function to be minimized is

$$F = \sum_{i=1}^{m}[V_i^{\mathrm{MEP}} - \sum_{j=1}^{n}(q_j/r_{ij})]^2 + \sum_{j=1}^{4}\lambda_j G_j \tag{A1}$$

where m is the number of sampling points, the total charge constraint is

$$G_1 = \sum_{j=1}^{n} q_j - q_{\mathrm{tot}} = 0 \tag{A2}$$

and the dipole moment constraints are of the form

$$G_2 = \sum_{j=1}^{n} q_j x_j - d_x = 0 \tag{A3}$$

with similar expressions for the y and z components G_3, G_4, and **d** is the quantum-mechanical dipole moment. Use of the variational principle to obtain the minimum of the least squares problem yields a set of linear equations of the form

$$\mathbf{A}\mathbf{Q} = \mathbf{B} \tag{A4}$$

where **Q** is a column vector of the n best fit point charges (augmented by the four LaGrange multipliers)

$$\mathbf{A}_{jk} = \sum_{i=1}^{m}(r_{ij}r_{ik})^{-1} \tag{A5}$$

is a square matrix (augmented by the constraint equations) and **B** is a column vector

$$\mathbf{B}_k = \sum_{i=1}^{m} V_i^{\mathrm{MEP}}(r_{ik})^{-1} \tag{A6}$$

(augmented by the total charge q_{tot}, and components of the dipole moment $d_{x,y,z}$).

The matrix **A** can be inverted by first decomposing it into a product

$$\mathbf{A} = \mathbf{U}\,\mathbf{W}\,\mathbf{V}^{\mathrm{T}} \tag{A7}$$

where **U** and **V** are orthogonal matrices and **W** is diagonal with elements w_j. Inversion gives

$$\mathbf{A}^{-1} = \mathbf{V}[\mathrm{diag}(w_j^{-1})]\mathbf{U}^{\mathrm{T}} \tag{A8}$$

The w_j are called the singular values of the matrix **A**, and the ratio of the largest to the smallest element w_j is the condition number of the matrix. If one or more of the w_j are zero, the condition number is infinite, and **A** does not have a unique and well-defined inverse. More commonly, the condition number may be large but finite. The small singular values correspond to directions in parameter space $\vec{V}_i$ (columns of the matrix **V**) along which the parameter values become increasingly uncertain. The method of singular value decomposition (SVD) involves

---

[82] Langen, R.; Jensen, G. M.; Jacob, U.; Stephens, P. J.; Warshel, A. *J. Biol. Chem.* **1992**, *267*, 25625−25627.

[83] Smith, E. T.; Tomich, J. M.; Iwamoto, T.; Richards, J. H.; Mao, Y.; Feinberg, B. A. *Biochemistry* **1991**, *30*, 11669−11676.

[84] Correll, C. C.; Ludwig, M. L.; Bruns, C. M.; Karplus, P. A. *Protein Sci.* **1993**, *2*, 2112−2133.

[85] Chen, J. L.; Noodleman, L.; Case, D. A.; Bashford, D. *J. Phys. Chem.* **1994**, *98*, 11059−11068.

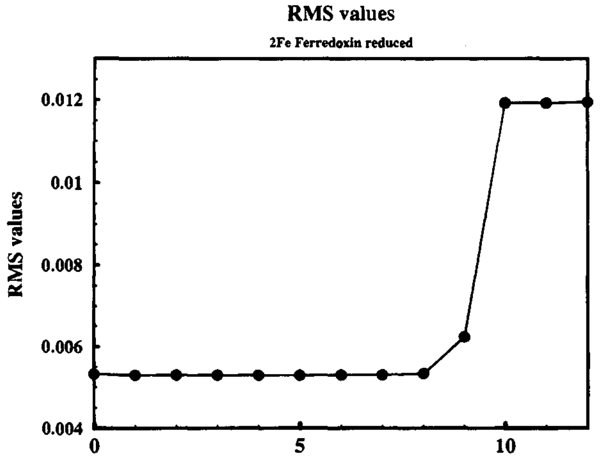

Figure 6. RMS deviation of the ESP charges fitted to the electrostatic potential for $[Fe_2S_2(SCH_3)_4]^{3-}$. Units = 1 au/e$^-$ = 27.21 V; 0.001 au/e$^-$ = 0.0272 V.

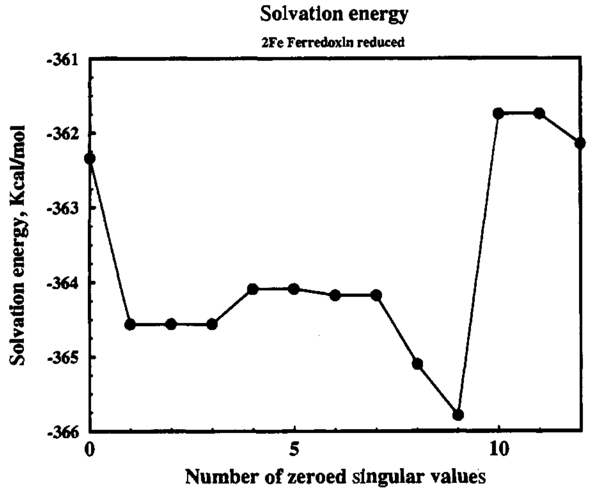

Figure 7. Total solvation energy of $[Fe_2S_2(SCH_3)_4]^{3-}$ vs number of SVD charges set to zero.

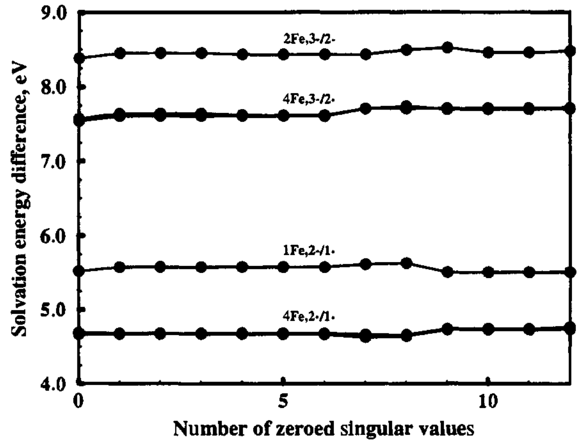

Figure 8. Solvation energy difference (ox-red, with ϵ = 37) for $[Fe(SCH_3)_4]^{1-,2-}$, $[Fe_2S_2(SCH_3)_4]^{2-,3-}$, $[Fe_4S_4(SCH_3)_4]^{2-,3-}$ (reduced couple states, OC1 and OC2, not distinguishable on this scale) and $[Fe_4S_4(SCH_3)_4]^{1-,2-}$ (oxidized high potentials, OS1, OS2, and OS3, also not distinguishable).

constructing a set of approximate solutions for the column vector **Q** as

$$\mathbf{Q} = \mathbf{V}[\mathrm{diag}(w_j^{-1})]\mathbf{U}^T\mathbf{B} \qquad (A9)$$

When w_j is either zero or sufficiently small, one replaces the corresponding w_j^{-1} by zero in the equation above. Further, when the w_j are placed in increasing order, and successively set to zero, one arrives at a sequence of charge models where the estimate of the relative probable error in the charge parameters decreases as the quality of the overall fit to the data (RMS of the fit) also decreases. In many cases, eliminating contributions for small w_j values causes only a marginal decrease in the quality of the fit while reducing the sensitivity and expected uncertainty of the fitted charges. We have found for the FeS systems under study that keeping all the w_j values or setting a few of the w_j^{-1} to zero yields quite similar atom charges and solvation energy differences.

The principal goal of the SVD analysis is to extract a sequence of charge fit models which can then be compared in various respects. We will compare (1) the quality of the fit to the data (root mean square, RMS), (2) conservation of total charge, (3) variations in the charge fit model, and (4) variations in the calculated solvation energies as the number of singular values set to zero is increased. In all cases tested, the RMS fit to the data was quite stable, or even improved slightly within the interval from 0 to 8 singular values set to zero.

As a representative example, results for 2Fe2S reduced are given in Figures 6 and 7 for the RMS of the charge fit to the electrostatic potential and the solvation energy versus the number of SV's set to zero. After 8 SV's, the RMS error shows a rapid rise. Because the SVD procedure gives an overall best fit, the charge constraint equation need not be exactly satisfied. A slight violation of charge conservation of −0.0075 e out of a charge of −3 is found when one or more SV's are zeroed, and is accompanied by a small decrease in the RMS. Figure 7 shows that the calculated solvation energy is reasonably stable for 0 to 8 zeroed singular values, the variation being at most 2.8 kcal/mol (0.12 eV). This behavior is typical for the systems we have studied. For a more complete view of the charge models, Figures S1−S6 in the supplemental material show that the predicted charges are quite stable using from 0 to 8 zeroed singular values, the methyl group charges being treated as a whole. Figure 8 shows the calculated variability in the solvation energy difference (ΔE_{PB}; oxidized minus reduced species) versus the number of zeroed singular values for all the clusters and electronic states studied. Again, the typical variability is about 0.1 eV, which gives us confidence in the numerical stability of the SVD algorithm. Therefore, any charge model in the 0 to 8 zeroed SV range gives similar results for charges, and we use values determined with no ignored singular values in the main text.

Supplementary Material Available: Supplemental figures (S1−S6) and atomic basis sets (13 pages). This material is contained in libraries on microfiche, immediately follows this article in the microfilm version of the journal, and can be ordered from the ACS; see any current masthead page for ordering information.